

The MJO and Air-Sea Interaction in TOGA COARE and DYNAMO

The Faculty of Oregon State University has made this article openly available.
Please share how this access benefits you. Your story matters.

Citation	de Szoeke, S. P., Edson, J. B., Marion, J. R., Fairall, C. W., & Bariteau, L. (2014). The MJO and Air-Sea Interaction in TOGA COARE and DYNAMO. <i>Journal of Climate</i> , 28(2), 597-622. doi:10.1175/JCLI-D-14-00477.1
DOI	10.1175/JCLI-D-14-00477.1
Publisher	American Meteorological Society
Version	Accepted Manuscript
Terms of Use	http://cdss.library.oregonstate.edu/sa-termsofuse

1 **The MJO and Air-Sea Interaction in TOGA COARE and DYNAMO**

2

3 Simon P. de Szoeke¹, James B. Edson², June R. Marion¹, Christopher W. Fairall³, and

4 Ludovic Bariteau³

5

6 ¹College of Earth, Ocean, and Atmospheric Science

7 104 CEOAS Admin Building

8 Oregon State University

9 Corvallis, OR 97331

10 sdeszoek@coas.oregonstate.edu

11

12 ²University of Connecticut, Avery Point

13 1080 Shennecossett Road

14 Groton, CT 06340

15

16 ³NOAA Earth System Research Laboratory/Physical Sciences Division

17 325 Broadway

18 Boulder, CO 80305

19

20

Abstract

21 DYNAMO and TOGA-COARE observations and reanalysis-based surface flux products are
22 used to test theories of atmosphere-ocean interaction that explain the Madden-Julian
23 Oscillation (MJO). Negative intraseasonal outgoing longwave radiation, indicating deep
24 convective clouds, is in phase with increased surface wind stress, decreased solar heating,
25 and increased surface turbulent heat flux—mostly evaporation—from the ocean to the
26 atmosphere. Net heat flux cools the upper ocean in the convective phase. Sea surface
27 temperature (SST) warms during the suppressed phase, reaching a maximum before the onset
28 of MJO convection. The timing of convection, surface flux, and SST is consistent from the
29 central Indian Ocean (70°E) to the western Pacific Ocean (160°E).

30

31 Mean surface evaporation observed in TOGA COARE and DYNAMO (110 W m^{-2}) accounts
32 for about half of the moisture supply for the mean precipitation (210 W m^{-2} for DYNAMO).
33 Precipitation maxima are an order of magnitude larger than evaporation anomalies, requiring
34 moisture convergence in the mean, and on intraseasonal and daily time scales. Column-
35 integrated moisture increases 2 cm before the convectively active phase over the research
36 vessel *Revelle* in DYNAMO, in accord with MJO moisture recharge theory. Local surface
37 evaporation does not significantly recharge the column water budget before convection. As
38 suggested in moisture mode theories, evaporation increases the moist static energy of the
39 column during convection. Rather than simply discharging moisture from the column, the
40 strongest daily precipitation anomalies in the convectively active phase accompany
41 increasing column moisture.

42 **1. Introduction**

43

44 The Madden Julian Oscillation is the leading intraseasonal (30-60 day) mode of atmospheric
45 variability of the equatorial atmosphere (Madden and Julian 1971, reviewed in Waliser 2006).

46 It is comprised of alternating zonal wind anomalies in the lower and upper troposphere of
47 planetary zonal scale. Deep convection accompanies surface convergence and upper level
48 divergence, and suppressed convection accompanies surface divergence. The 30-60 day time
49 scale of the MJO is long compared to the time scale of atmospheric convection, and it
50 propagates eastward at 5 m s^{-1} .

51

52 The long time scale of the Madden Julian Oscillation (MJO) and its slow propagation
53 compared to the observed time scales of atmospheric convection and propagation speeds of
54 equatorial waves remains unexplained by theoretical models. Most commonly cited models
55 explain low-level convergence by unbalanced diabatic heating by convection (*wave-CISK*,
56 Conditional Instability of the Second Kind; e.g. Gill 1980, Lau and Peng 1987; or boundary-
57 layer frictional wave-CISK, e.g. Wang and Rui 1990, Salby et al. 1994), or by a *quasi-*
58 *equilibrium* between circulation and radiative-convective equilibrium (Neelin et al. 1987;
59 Emanuel 1987; Neelin and Zeng 2000). Other models with nonlinear interaction of smaller
60 scale waves, e.g. through triggering convection, predict organization of synoptic-scale
61 convection into a large MJO envelope (Majda and Stechmann 2009; Yang and Ingersoll
62 2013). The waves predicted by wave-CISK propagate faster than the MJO, and the shortest
63 waves are the most unstable to wave-CISK (Hendon 2005). Frictional wave-CISK predicts
64 slower waves destabilized by boundary layer moist static energy convergence. Convectively
65 coupled equatorial Kelvin, Rossby, and inertia-gravity waves are observed with higher

66 frequencies and smaller scales that do not match the planetary scale of the MJO (Wheeler and
67 Kiladis 1999).

68

69 Quasi-equilibrium models assume that latent heating above precipitation is balanced by
70 adiabatic cooling of buoyant rising air (e.g. Riehl and Malkus 1958), and convection quickly
71 redistributes moist static energy anomalies from the boundary layer throughout the
72 troposphere to an equilibrium temperature profile. Neelin et al. (1987) and Emanuel (1987)
73 developed quasi-equilibrium models with wind-evaporation or wind induced surface heat
74 exchange (WISHE) to explain growth and eastward propagation of convective anomalies. In
75 WISHE, evaporation from the ocean surface is enhanced under stronger wind speeds to the
76 east of the maximum upward velocity anomaly for easterly mean winds. Contrary to the
77 eastward propagation of the MJO, the original WISHE theory predicts westward propagation
78 of disturbances for the mean westerlies found over the Indian and western Pacific Ocean.

79

80 Under weak planetary rotation (implying large Rossby radius of deformation) gravity waves
81 efficiently redistribute temperature anomalies throughout the tropics. The resulting relatively
82 homogeneous temperature structure observed in the tropical free troposphere is modeled by
83 the weak temperature gradient (WTG) assumption (Sobel and Bretherton 2000, Sobel et al.
84 2001). Even in the case of weak temperature gradients, moisture anomalies increase the moist
85 static energy of the tropospheric column (e.g. Maloney et al. 2009). *Moisture mode* theories
86 for the MJO consider the feedback between moisture anomalies and convection (Sugiyama
87 2009, Hannah and Maloney 2014, Benedict et al. 2014). The quasi-equilibrium moisture
88 mode grows when there is an alignment between precipitation and net column heating.

89

90 No single theory has been accepted that links tropical convection and large-scale equatorial
91 waves yielding anomalies on the time and spatial scale of the MJO. It has been suggested that
92 the thermal inertia of the upper ocean may play a role in setting the intraseasonal time scale
93 and slow propagation of the MJO (e.g. Krishnamurti et al. 1988). Although MJO variability
94 is found in some uncoupled simulations from atmospheric general circulation models, in
95 many models coupled SST makes intraseasonal anomalies more closely resemble observed
96 intraseasonal variability (Flatau et al. 1997, Waliser et al. 1999, Inness and Slingo 2002,
97 Benedict and Randall 2011, DeMott et al. 2014). Atmospheric GCMs coupled to SST in slab
98 ocean models improve predictability of intraseasonal variability compared to atmosphere-
99 only general circulation models (Woolnough et al. 2007).

100

101 Intraseasonal air-sea interaction plays an important role on the stage of the warm pool of the
102 Indian and Pacific Oceans ($SST > 28.5^\circ\text{C}$, Figure 1a). The standard deviation of intraseasonal
103 outgoing longwave radiation (OLR) anomalies contoured in Figure 1a has maxima over both
104 the Indian Ocean and western Pacific Ocean sectors of the warm pool, with lower amplitude
105 over the Maritime Continent, particularly over the islands. Though the intraseasonal
106 variability of zonal wind stress (Figure 1b) is larger away from the equator, it also has two
107 saddles of high variability bridging the equator to the east and west of the Maritime
108 Continent. Figure 1b shows annual wind stress climatology from the Satellite Climatology of
109 Ocean Winds (Risien and Chelton 2008) as vectors. The zonal wind stress is shaded. The
110 zonal wind stress is westward throughout most of the tropics, but high intraseasonal
111 variability in zonal wind stress and convection coincides with regions of warm SST and
112 eastward mean winds near the equator. Locations of Dynamics of the Madden Julian
113 Oscillation (DYNAMO, Yoneyama et al. 2013) in the central Indian Ocean, and Tropical
114 Ocean Global Atmosphere Coupled Ocean Atmosphere Response Experiment (TOGA

115 COARE, Webster and Lukas 1992) in the western Pacific Ocean, are marked with stars on
116 Figure 1.

117

118 Three MJO convective events and their accompanying air-sea interactions were observed in
119 TOGA COARE in 1992. Analyses of TOGA COARE observations and composites from
120 reanalysis data showed wind speed and evaporation anomalies following OLR anomalies that
121 indicate deep convection (Hendon and Glick 1997; Shinoda et al. 1998; Woolnough et al.
122 2000). Longer in situ records from TAO buoys show westerly wind bursts and evaporation
123 considerably more synchronous with convection on average than was found for the
124 reanalyses or the three events of TOGA COARE (Zhang and McPhaden 2000). SST
125 decreased beneath the increased evaporative cooling and reduced solar radiation on the ocean
126 surface. Though evaporation was enhanced in convective events, peak precipitation in
127 convective events was 3-5 times greater than the rate of surface evaporation in TOGA
128 COARE (Lin and Johnson 1996), with moisture convergence supplying most of the moisture
129 for the precipitation.

130

131 We observed equatorial intraseasonal air-sea interaction in the central Indian Ocean during
132 DYNAMO. In this paper we assess the response of surface fluxes and SST to intraseasonal
133 convective anomalies, examining the evidence that intraseasonal interaction of the
134 atmosphere with surface fluxes, or with the SST, is a significant contributor to the MJO. We
135 use TOGA COARE and DYNAMO observations, and surface flux products based on global
136 reanalyses. From these data sets we assess three hypothetical models of ocean-atmosphere
137 interactions:

138

139 1) *Intraseasonal surface flux feedback*: Intraseasonal atmospheric variability, primarily wind
140 speed and clouds, affects surface heat fluxes (mostly evaporation), contributing to boundary
141 layer moist static energy fluctuations that destabilize the atmosphere to intraseasonal
142 convective modes (which might be wave-CISK, or frictional wave-CISK, or moisture modes).
143 In this process, surface fluxes are modulated by intraseasonally changing meteorological
144 variables, whether or not the ocean responds to the changing conditions. (Neelin et al. 1987,
145 Emanuel 1987, Weller and Anderson 1996, Sugiyama 2009, Sobel et al. 2010, Sobel and
146 Maloney 2012)

147

148 2) *Coupled ocean-atmosphere interaction*: Intraseasonal atmospheric variability modifies sea
149 surface temperature (SST) and ocean mixed layer depth. Intraseasonal changes in the wind
150 strongly modulate the surface fluxes, ocean mixing, mixed layer depth, and heat storage by
151 the ocean. The heat stored in the upper ocean affects surface fluxes and feeds back to
152 atmospheric convection. (Hendon and Glick 1997, Wang and Xie 1998, Woolnough et al.
153 2000, Inness and Slingo 2003, Marshall et al. 2007)

154

155 3) *Atmospheric moisture recharge*: Moisture builds up in the atmospheric column,
156 particularly the lower free troposphere, in the convectively suppressed phase. This moisture
157 preconditions the atmosphere for subsequent convective anomalies. Anomalous precipitation
158 in the convectively active phase discharges moisture from the atmospheric column,
159 suppressing convection until the column moisture can recharge again. Moisture recharge in
160 the suppressed phase could be due to evaporation, horizontal convergence of water vapor, or
161 vertical transport of moisture by shallow cumulus or cumulus congestus clouds that detrain
162 water in the mid-troposphere. (Bladé and Hartmann 1993, Kemball-Cook and Weare 2001,
163 Benedict and Randall 2009)

164

165 In Section 2 we introduce the DYNAMO and TOGA COARE in situ observations and assess
166 the OAFlux and TropFlux surface flux data sets against them. Appendix A provides a
167 detailed description of each variable in DYNAMO surface meteorology and flux data set
168 from the research vessel *Roger Revelle*. The methods used for isolating and compositing
169 equatorial waves and the MJO are described in section 3, with more details in Appendix B.

170

171 In Section 4 we present observed time series of daily and sub-daily variability from
172 DYNAMO and TOGA COARE, and analysis of 27 years of the daily time-longitude
173 structure air-sea interaction variables and in relation to the MJO. Section 5 presents a
174 discussion of the contribution of the surface flux and SST variation to MJO convective
175 anomalies and Section 6 concludes the paper.

176

177 **2. Data**

178

179 *DYNAMO*

180 We use in situ time series observations collected from the research vessel *Roger Revelle* in
181 the DYNAMO experiment intensive observation period. The DYNAMO *Revelle* sampling
182 consisted of four research cruises (Moum et al. 2014). We present the surface meteorology
183 and air-sea flux data from legs 2-4 (2011 October 3-December 31) when the ship spent
184 considerable time on the equator in the vicinity of 80.5° E.

185

186 Oregon State University, University of Connecticut, and NOAA Earth System Research
187 Laboratory Physical Sciences Division (ESRL PSD) deployed parallel surface meteorology
188 and covariance flux systems on the forward mast of the *Revelle* (similar to shipboard systems

189 described in Fairall et al. 1997). Together these systems measured mean air temperature,
190 humidity (at 15 m above sea level), vector wind (~20 m), sea surface temperature at 0.1 m
191 depth (SST), and downwelling solar and longwave infrared radiative fluxes each minute. The
192 DYNAMO observations are described further in Appendix A. Unless otherwise noted, in this
193 paper we use 10-minute averages of the DYNAMO surface meteorology and flux variables.
194 Fluxes shown herein are computed from the 10-minute averages with the COARE version 3.5
195 bulk aerodynamic formula (Fairall et al. 1996, Fairall et al. 2003, Edson et al. 2013).

196

197 Meteorological, sea-air interface, and upper ocean variables are available in the DYNAMO
198 *Revelle* meteorology and flux group data set (<ftp://dynamo.dms.uconn.edu/> linked from the
199 EOL field catalog http://data.eol.ucar.edu/master_list/?project=DYNAMO). These variables
200 and the techniques used to process them are further described in Appendix A.

201

202 *TOGA COARE*

203 We use Tropical Ocean Global Atmosphere Coupled Ocean Atmosphere Response
204 Experiment (TOGA COARE) observations from the R/V *Moana Wave* and Woods Hole
205 Oceanographic Institution (WHOI) Improved Meteorological Packages (IMET) buoy (Weller
206 et al. 1996, Anderson et al. 1996, available at <http://rda.ucar.edu/datasets/ds606.1/>). Similar
207 data to the DYNAMO data described above were collected on the R/V *Moana Wave* (Fairall
208 et al. 1997). Meteorological and oceanographic data from the IMET buoy were averaged
209 hourly. Because precipitation is unevenly distributed and it is difficult to obtain a
210 representative sample from single rain gauges, we use the average of gauges on the IMET
211 buoy, the NOAA Tropical Atmosphere Ocean (TAO) buoy at 2°S, and the research vessels
212 *Moana Wave* and *Wecoma*, (Anderson et al. 1996).

213

214 *Outgoing Longwave Radiation*

215 Convectively coupled equatorial waves are diagnosed using principal component analysis
216 and compositing using daily NOAA Interpolated Outgoing Longwave Radiation (OLR) data
217 interpolated to 2.5°x2.5° resolution (Liebmann and Smith 1996, available from NOAA ESRL
218 PSD http://www.esrl.noaa.gov/psd/data/gridded/data.interp_OLR.html). We use the 27.5 year
219 period of data without gaps from 1985 January to 2012 June. OLR data indicate the depth
220 and/or frequency of deep convection. Daily data are suitable to diagnose intraseasonal MJO
221 variability, convectively coupled equatorial Kelvin waves, and convectively coupled
222 equatorial Rossby waves (Wheeler and Kiladis 1999).

223

224 *TropFlux and OAFlex gridded surface flux products*

225 We supplement the surface flux observations from DYNAMO and TOGA COARE with
226 1°x1° spatially resolved TropFlux air sea fluxes for the tropical oceans and OAFlex
227 objectively analyzed surface flux data. TropFlux (Praveen Kumar 2012;
228 <http://www.incois.gov.in/tropflux/>) uses bias-corrected ECMWF Interim Reanalysis (ERA-I)
229 variables to compute fluxes. The SST, air temperature, air humidity, and wind speed
230 variables from ERA-I were adjusted to remove biases compared to TAO, PIRATA, and
231 RAMA buoy observations before computing fluxes with the COARE version 3.0 bulk flux
232 algorithm. Neither the effect of the diurnal solar warm layer, nor the effect of the cool
233 viscous sublayer on SST, is implemented in the TropFlux bulk flux computations.

234

235 OAFlex (Yu and Weller 2007) uses optimal analysis (OA) of two meteorological reanalysis
236 products (NCEP/DOE Reanalysis 2, Kalnay et al. 1996, Kanamitsu 2002; and ERA 40-year
237 Reanalysis, Uppala et al. 2005) and satellite SST and wind speed observations to provide
238 inputs for the COARE 3.0 bulk flux algorithm. The optimal analysis of the flux input

239 variables is found by minimizing a cost function of a weighted sum of differences between
240 the analysis and model data and satellite observations. OAFlux uses in situ observations from
241 buoys and ships collected in the Comprehensive Ocean Atmosphere Data Set (COADS,
242 Woodruff et al. 1998) to estimate the errors in the satellite and reanalysis estimates. In situ
243 data from buoys and ship observations enter TropFlux and OAFlux through assimilation into
244 the NCEP/DOE, ERA-40, and ERA-I reanalyses.

245

246 Intraseasonal (30-90 day) net surface heat flux standard deviation is about 20 W m^{-2} for
247 either OAFlux or TropFlux over the Indian Ocean thermocline ridge (50° - 80° E and 12° - 5° S;
248 Praveen Kumar, 2012, Figure 15c). The daily gridded surface flux products agree well with
249 in situ observations during DYNAMO and TOGA COARE. Figure 2 shows the agreement of
250 daily latent and sensible heat flux with measurements made aboard the *Revelle* in DYNAMO,
251 and with the measurements aboard the R/V *Moana Wave* in TOGA COARE. TropFlux and
252 OAFlux overestimate TOGA COARE latent heat flux by 30 and 20 W m^{-2} , respectively.
253 TropFlux underestimates the TOGA COARE mean sensible heat flux by 1 W m^{-2} .

254

255 The reanalyses used by the gridded flux products in Figure 2 resolve the main features of
256 daily variability. Daily TropFlux and OAFlux latent and sensible heat fluxes are correlated at
257 0.84 and 0.87 with the DYNAMO ship observations; and correlated 0.72 and 0.83 with the
258 TOGA COARE ship observations. The success of TropFlux and OAFlux at reproducing the
259 DYNAMO ship observations at 0° N, 80.5° E may be due to the reanalyses assimilating data
260 from the nearby RAMA buoy (0° N, 80.5° E ~ 2 km from the *Revelle*), and the slightly more
261 distant RAMA buoys at 80.5° E, 1.5° S and 1.5° N. The standard deviation of the sensible heat
262 flux is almost as large as the mean sensible heat flux ($7\text{-}8 \text{ W m}^{-2}$). The standard deviation of
263 TropFlux latent heat flux was 30 W m^{-2} for DYNAMO and 40 W m^{-2} for TOGA COARE.

264 TropFlux and OAFlux overestimate the standard deviation of the latent heat flux by 14% and
265 8% respectively in TOGA COARE, and 20% and 8% in DYNAMO. Mean sensible and
266 latent heat fluxes, their standard deviations, and their correlation with the ship observations
267 for DYNAMO are tabulated in Table 1.

268

269 Surface radiative fluxes are provided in OAFlux and TropFlux by the International Satellite
270 Cloud Climatology Project (ISCCP) Flux Data set (ISCCP FD, Zhang et al. 2004). TropFlux
271 adjusts ISCCP FD for mean and amplitude biases relative to the buoy observations. Radiative
272 surface fluxes from ISCCP FD match surface observations better than radiative fluxes from
273 reanalysis. ISCCP FD is updated irregularly (available until 2009 at the time of writing), so
274 TropFlux uses bias-corrected surface longwave fluxes from ERA-I reanalysis when ISCCP
275 FD is not available. TropFlux “real-time” solar radiation is derived as the ISCCP FD bias-
276 corrected climatology plus an anomaly of 1.32 times the anomalous OLR (similar to Shinoda
277 et al. 1998). Solar radiation derived in this way fits the mean and amplitude of surface
278 observations well, however it is clearly not independent of the OLR data.

279

280 We also use the ERA-I (Dee et al. 2011) SST product provided with TropFlux on the $1^{\circ} \times 1^{\circ}$
281 degree grid. The ERA-I air temperature is consistent with this SST, according to the physics
282 of the ERA-I model. ERA-I uses NCEP 7-day optimally interpolated SST (OI SST, Reynolds
283 et al. 2002) for 1989-2001 and daily Operational Sea Surface Temperature and Sea Ice
284 Analysis (OSTIA, Donlon et al. 2012) from 2009 to the time of writing.

285

286 **3. Methods**

287

288 We isolate intraseasonal variability in OLR, then composite the surface flux variables on the
289 OLR based index. We select symmetric MJO variability with a meridional average over
290 15°S-15°N. Intraseasonal variability is isolated from 27.5 years (1985-2012) of continuous
291 daily satellite OLR observations and the TropFlux and OAFlux surface fluxes with a 6th
292 order Butterworth band pass filter with cutoff frequencies corresponding to periods of 15 to
293 100 days. We choose this relatively wide range of frequencies in order not to constrain the
294 spectral characteristics of intraseasonal variability too narrowly.

295

296 *Principal component analysis*

297 We use principal component analysis (PCA) to isolate and diagnose the phase of the MJO
298 (e.g. Shinoda et al. 1998, Wheeler and Hendon 2004, Kiladis et al. 2014). We perform PCA
299 on the intraseasonally filtered $\pm 15^\circ\text{N}$ OLR time-longitude matrix. The PCA separates the
300 time-longitude matrix into orthogonal spatial and temporal modes of variability. Each mode
301 is separated into a spatial empirical orthogonal function (EOF, Figure 3a-d) and a temporal
302 principal component (PC) time series (Figure 3e-h). Superposition of all modes recovers the
303 entire time-longitude input data matrix. OLR varies most in the climatologically convective
304 regions of the Indian Ocean and Western Pacific Ocean, so the PCA selects modes that
305 explain variability in that region.

306

307 The first two principal components explain significantly more variance (21 and 16%) of the
308 OLR data than the following principal components. The two PCs are nearly in quadrature,
309 co-propagating from west to east (Figure 3). These two PCs are statistically distinct from the
310 other PCs but not distinct from each other by the criterion of North et al. (1982). We retain
311 only the first two PC time series as an efficient representation of eastward propagating MJO

312 events. The time-longitude structure of MJO is diagnosed by the product of the PC time
313 series with the OLR EOFs, and with the spatial projections of the surface flux variables.

314

315 The truncated PC time series were normalized to have unity standard deviation, and the EOFs
316 normalized so that they represent the spatial OLR pattern (W m^{-2}) projected for a normalized
317 PC anomaly of 1. The surface wind stress, and sensible, latent, solar, and longwave heat
318 fluxes were regressed onto the first two normalized PC time series to yield their spatial
319 pattern (Figure 3e-h).

320

321 The compositing procedure described in Appendix B uses the phase of the MJO described by
322 the angle of the vector formed from the first two principal components. The result of the
323 analysis is essentially the same for OAFlux so we show only TropFlux for brevity.

324

325

326 **4. Results**

327

328 *Global and local intraseasonal variability of OLR and SST*

329 First we analyze the intraseasonal variability of OLR and SST during the DYNAMO (0°N ,
330 80.5°E , from 2011 October-2012 January) and TOGA COARE (1.8°S , 156°E , 1992 October-
331 1993 March) field experiments. Intraseasonal coupled atmosphere-ocean interaction ought to
332 be reflected in variability of both atmospheric convection (OLR) and SST. Time series of
333 daily OLR are traced by blue lines in Figure 4a,c. Sea surface temperature time series from
334 ERA-I (daily for DYNAMO, weekly for TOGA COARE) are shown in Figure 4b,d.
335 Intraseasonal (15-100 day filtered) variations of OLR and SST (thick blue lines, Figure 4)
336 indicate three local intraseasonal minima in OLR in the central Indian Ocean during

337 DYNAMO. These minima of OLR, labeled *I1*, *I2*, and *I3*, indicate times when active
338 convection drove cloud tops deep in the cold upper troposphere. These events were
339 accompanied by decreasing SST and net upward surface heat flux, so that each minimum in
340 OLR was followed by a minimum in SST within 2-10 days. Table 2 shows the dates of the
341 identified intraseasonal events.

342

343 OLR was low over the West Pacific TOGA COARE experiment for two 10-20 day intervals,
344 labeled *P1* and *P2* on Figure 4c,d. A third period of modestly decreasing SST in TOGA
345 COARE at the end of January 1993 (*P3*) has a weak minimum of intraseasonal OLR. The
346 projections of the PCA and Realtime Multivariate MJO (RMM, Wheeler and Hendon 2004)
347 indices indicate the canonical planetary intraseasonal structure associated with low OLR at
348 1.8°S , 156°E is present for *P3*. SST has weaker variability than OLR on shorter time scales.
349 The NCEP SST used by ERA-I in 1992-1993 is only weekly, so for a fairer comparison to
350 the daily SST in DYNAMO, we use NOAA Optimally Interpolated version 2 daily SST
351 (Reynolds et al. 2007) at the TOGA COARE location in Figure 4d.

352

353 Local time series show the local effects of daily and intraseasonal variability on OLR and
354 SST (Figure 4). The magnitude of the vector formed from the first two PCs is about 1.5
355 standard deviations for most of DYNAMO as shown by gray dashed line in Figure 4. In
356 TOGA COARE the magnitude of the PCs has one long enhancement with a maximum of 3.4
357 standard deviations in January 1993.

358

359 The two PCs efficiently representing the MJO on a global scale are correlated to the local
360 intraseasonal variability, but their local peak-to-trough range in DYNAMO is only 56% of
361 the range of the daily time series, and only 80% of the intraseasonally filtered OLR range

362 (Table 3). The local peak-to-trough range indicates the strength of local extrema in late 2011,
363 but is not representative of the amount of variance explained. The range of the RMM
364 projection is only 30% of the local intraseasonal OLR peak-to-trough range. Regressions of
365 the OLR PC or the RMM index underpredict the local SST range even more. Therefore,
366 much of the observed intraseasonal variability in the DYNAMO and TOGA COARE
367 observations is due to local or regional phenomena that are not closely linked to the global-
368 scale development and propagation of the MJO.

369

370 *DYNAMO and TOGA COARE time series*

371 We next present time series from DYNAMO observations from the R/V *Revelle* at the
372 equator, 80.5°E (Figure 5). The intraseasonal minima of OLR (I1, I2, and I3) are associated
373 with negative net surface heat flux, clouds and rain, eastward wind stress, cooler air
374 temperature, and decreasing SST. The timing of strong individual rain, stress, or heat flux
375 events can differ by up to several days from the time the intraseasonal OLR reaches a
376 minimum.

377

378 Figures 5 and 6 are modeled after Figure 3 of Anderson et al. (1996). Figure 5a shows daily
379 average solar, latent, sensible, and net heat fluxes. As over most of the tropical oceans, the
380 net downwelling surface solar radiation was the only term of the surface fluxes that warms
381 the ocean. Its mean exceeded 200 W m^{-2} on most days, larger than the sum of sensible, latent,
382 and net longwave radiative flux cooling the ocean. The average heat flux gained by the ocean
383 at the surface during the 3 *Revelle* deployments to the equator was 43 W m^{-2} . Days with
384 negative net heat flux (highlighted with pale green bars) corresponded to convective
385 conditions.

386

387 Clouds extinguished the incoming solar radiation, usually to less than 100 W m^{-2} , for all of
388 the days of negative net surface heat flux. The blue shaded area in Figure 5b corresponds to
389 hourly clear-sky fraction (the white area extending from the top of the axis corresponds to the
390 cloud fraction). Less cloud fraction corresponds to more daily average solar radiation (Figure
391 5a). Some of the clouds were dynamically vigorous enough to rain. Figure 5b shows the daily
392 average rain rate averaged over the (1257 km^2) area within 20 km of the ship from the
393 Colorado State University TOGA radar (Thompson et al. 2014, gray bars) and sampled by
394 the PSD rain gauge on the ship (gray circles). The maximum daily rain sampled on the ship
395 in the 3 legs was 7.5 mm h^{-1} on 2011 October 28. On these days there was reduced solar
396 radiation and net surface cooling of the ocean surface. Because rain is notoriously unevenly
397 distributed, the rain at the gauge on the ship was subject to considerable variability, yet the
398 daily rain rate from the radar area corresponded well ($r=0.64$) to the rain measured on the
399 ship.

400

401 Most days with negative net surface heat flux also had stronger zonal wind stress. (The wind
402 stress magnitude is correlated to the zonal wind stress magnitude at $r=0.98$, and meridional
403 wind stress is strongly correlated with zonal wind stress.) Mean zonal wind stress for the
404 *Revelle* deployment on the equator in DYNAMO was $0.028 \pm 0.005 \text{ N m}^{-2}$ eastward (i.e., a
405 mean westerly wind). Unlike westward stress under trade winds, which drives equatorial
406 upwelling, the mean eastward wind stress drives Ekman convergence on the equator,
407 resulting in equatorial downwelling. However, the zonal wind stress occurs in short bursts
408 that last several days. Stress observations exceeded 0.2 N m^{-2} for a total of 27 hours (1.5% of
409 the time sampled) during DYNAMO and the peak stress was 1 N m^{-2} . Such (eastward)
410 westerly wind bursts can drive mixing of temperature and salinity across the thermocline
411 (Smyth et al. 1996), and accelerate zonal currents in the ocean, whose convergence initiates

412 downwelling waves in the equatorial thermocline that in the Pacific Ocean lead to equatorial
413 El Niño-Southern Oscillation (ENSO) anomalies (McPhaden et al. 1992).
414
415 Intraseasonal cycles of SST were observed on *Revelle* during the months of October and
416 November during DYNAMO. The ocean also responds thermodynamically to the surface
417 heat flux. SST increased gradually in the beginning of October, November, and December,
418 reaching maximum temperature at 0.1 m depth on the afternoons of 2011 October 15,
419 November 16, and probably during the *Revelle's* port call and transit between legs 3 and 4
420 (Figure 5d). The SST cooled in the periods with negative net heat flux. The 0.1 m SST shows
421 strong diurnal warming during the periods of gradual SST warming, especially October 5-22
422 and November 11-23. Ocean temperature at 10 m depth (taken from the OSU Chameleon
423 profiler or the nearby UW/APL buoy when the *Revelle* was off station) was usually slightly
424 cooler and had a delayed and muted diurnal warming (consistent with the model of Price et al.
425 1986 and observations of Anderson et al. 1996). The warmest 10 m temperature occurred on
426 October 19 (excepting a 2 hour anomaly on October 16) and October 22, a few days later
427 than the peak temperature at 0.1 m. The 0.1 m ocean temperature was usually as warm or
428 warmer than the 10 m temperature, but there were brief exceptions. These times were
429 probably associated with rain deposited at the wet bulb temperature, which is colder than the
430 air temperature. During calm periods rain also freshened and stratified the upper few meters
431 of the ocean briefly, trapping the cooling of the surface heat fluxes within a shallow layer
432 (this shallow layer is still warmer than the atmosphere) without changing the vertical profile
433 of absorption of solar radiation.
434
435 Some days show no diurnal cycles of SST. On these days the temperature decreased at 0.1 m
436 and 10 m depth alike (Figure 5d). One or two days with no diurnal cycle of SST were found

437 in the intraseasonal slowly warming phase (October 13, 19), but most of the days with no
438 diurnal SST layer were in the cooling phase of the intraseasonal oscillation. Notably on
439 October 24-25 and 28-29, and on November 24-25 and 28-30 there was no diurnal warming.
440 These days also had negative daily average net surface heat (and buoyancy) flux, and strong
441 wind stress that quickly distributes solar heating throughout the upper ocean mixed layer. The
442 surface temperature without diurnal warming occurred atop two periods that the 10 m
443 temperature decreases on a longer time scale. In convective period I1 the 10 m depth ocean
444 temperature decreased -0.7° C from October 22-30, and in period I2 the temperature
445 decreased -1.3° C from November 22-December 1. Ocean temperature also varies due to
446 non-locally forced advection. Some temperature changes at 10 m (Figure 5, dark red) were
447 coherent with changes below the mixed layer (e.g. November 16-19) and unrelated to local
448 surface stress, heat flux, or the solar cycle (K. Pujiana, personal communication).

449

450 All DYNAMO convective events had eastward wind stress and cooled the ocean by net
451 upward surface heat flux, but each event had a unique progression of features. Event I1 had
452 the strongest precipitation at the ship. Event I2 had two distinct bursts of eastward wind stress,
453 each one associated with a burst of convection (Moum et al. 2014). Intraseasonal event I2
454 had two maxima of rain at the ship and two minima in daily OLR. According to time-
455 longitude plots from satellite retrievals of OLR and rain, these features of deep atmospheric
456 convection propagated eastward over the *Revelle* at $8-9 \text{ m s}^{-1}$ (Yoneyama et al. 2013, Moum
457 et al. 2014 Figure 3), the phase velocity expected for a convectively-coupled Kelvin wave
458 (Kiladis et al. 2009). The *Revelle* observed only the conclusion of convection from event I3.
459 This was then followed by the strongest wind stress observed in DYNAMO and a week-long
460 period of enhanced eastward wind stress without convective activity.

461

462 Air temperature measured on the ship (adjusted by flux-gradient similarity to 10 m height;
463 blue, Figure 5d) was considerably more variable than ocean temperature. Air temperature
464 roughly followed SST during weeks of warming in the convectively suppressed periods early
465 in each of the months of October, November, and perhaps December, with the air about 1°C
466 cooler than the SST. The air-sea temperature difference was even more negative in the
467 convective periods in late October and November. The air temperature dropped in brief
468 episodic cold pools, that can be identified by the air temperature dropping below 27°C. These
469 cold pools were asymmetric in time, with sudden cooling followed by a gradual recovery of
470 the temperature. Often the temperature dropped due to a second or multiple cold pools before
471 recovering from an earlier cold pool. Cold pools varied in strength and recovery time. There
472 were more and stronger cold pools during the convectively active phase of intraseasonal
473 variability. Cold pools increased surface sensible and latent heat fluxes (Yokoi et al. 2014,
474 Feng et al. 2014).

475

476 The role of the surface fluxes and westerly wind bursts during the TOGA COARE (1992
477 October-1993 March) experiment on the upper west Pacific Ocean has been well documented.
478 The 134-day time series from TOGA COARE IMET (1.8°S, 156°E; Weller and Anderson
479 1996, Anderson et al. 1996) and the R/V *Moana Wave* (1.7°S, 156°E for 1992 November 11-
480 December 3, December 17-January 11, and 1992 January 28-1993 February 16; Fairall et al.
481 1996a) observations are shown in Figure 6. Table 4 shows the mean net heat flux, the sum of
482 the cooling, and the solar warming, as well as the standard error of their mean for DYNAMO
483 and TOGA COARE. The mean net surface flux warming in TOGA COARE was only about
484 20 W m^{-2} , half the net surface warming observed in the central Indian Ocean in DYNAMO.
485 This was mostly due to stronger solar radiation in DYNAMO ($216 \pm 9 \text{ W m}^{-2}$) than in TOGA
486 COARE ($193 \pm 3 \text{ W m}^{-2}$). The average sum of latent, sensible, and longwave cooling is

487 statistically indistinguishable between DYNAMO and TOGA COARE. Standard error of the
488 mean net heat flux is larger than its constituents because daily solar and evaporation
489 anomalies are of the same sign, even though their means have opposite signs.

490

491 The intraseasonal convectively active events P1, P2, and P3 (defined by OLR minima) in the
492 western Pacific Ocean during TOGA COARE are indicated on Figure 6a and d. They
493 coincided with groups of days with negative net heat fluxes, some that reach -200 W m^{-2} . As
494 in DYNAMO, the diurnal cycle of SST was small during periods of enhanced wind stress and
495 negative net heat flux, and large when the wind was calm, e.g. on November 13-22
496 November 28-December 6, and January 8-16.

497

498 The event P2 stands out as an example of strong rainfall, eastward wind stress, and
499 evaporation. SST decreased for 24 days in the middle of TOGA COARE (1992 December
500 12-1993 January 5). Daily minimum SST at 0.45 m decreased by 1.5°C in P2. Zonal wind
501 blew eastward in 4 consecutive 5-day bursts separated by wind stress minima. The first three
502 were associated with convection. Daily average rain was greater than 1 mm h^{-1} for the first
503 three of these bursts. The final strong wind burst blew during a minimum of rainfall. From
504 December 26-January 3 strong solar radiation and evaporation due to the wind canceled,
505 finishing the long intraseasonal event P2 with small net heat fluxes weaker than 50 W m^{-2} .
506 This event was unusual in its strength and duration. Yet the continuation of the eastward
507 wind, which began during the time of convection and negative net heat flux, into the sunny
508 and weak net heat flux conditions following the convection, was typical of events in TOGA
509 COARE. Events P1 and P3 were followed by weak eastward wind stress and weak positive
510 heat flux during 1992 October 31-November 6 and 1993 February 2-9, respectively. In
511 DYNAMO, only convective event I3 was followed by strong wind stress after the convection

512 cleared. SST at the end of TOGA COARE was nearly constant over four quasi 7-day
513 synoptic vacillations between positive and negative net heat flux following P3. These
514 vacillations were apparently driven by bursts of eastward wind stress on time scales shorter
515 than the MJO, resulting in nearly simultaneous changes in the shortwave radiation and
516 evaporation. We can't confidently identify systematic differences between intraseasonal
517 events in the Indian Ocean and Western Pacific Ocean from the 3 diverse events sampled in
518 each basin.

519

520 Synoptic convective events were found inside and outside of the convective envelope of the
521 MJO in DYNAMO and TOGA COARE. For example, the 8-9 m s⁻¹ eastward propagation of
522 the two convective features in event I2 in DYNAMO suggests they were convectively-
523 coupled atmospheric Kelvin waves. Sounding anomalies on a 10-m vertical grid are
524 computed by removing the vertical 11-point moving average of all DYNAMO *Revelle*
525 soundings (Figure 7). As in Straub and Kiladis (2003, Figure 5) time progresses from right to
526 left in Figure 7 to emulate the zonal structure of the waves as they propagate eastward over
527 the *Revelle*. The time-vertical structure of temperature, humidity, and zonal wind from
528 rawinsondes released from *Revelle* in the two propagating wave features further resemble
529 composites of Kelvin waves over Majuro (7°N, 171°E; Straub and Kiladis 2003, Kiladis et al.
530 2009) in several respects: First, upper tropospheric temperature anomalies last about 2 days
531 for each convective burst of event I2. Second, strong upper tropospheric heating begins about
532 a day before the maximum tropospheric warm anomaly at 200 hPa (Figure 7a). Third,
533 specific humidity anomalies at 800-400 hPa lag the potential temperature anomaly by about 1
534 day. Zonal wind lags by an additional day and tilts westward with height. The eastward wind
535 starts abruptly and appears to coincide with the end of the highest specific humidity

536 anomalies. The propagation and vertical structure of the Kelvin waves were distinctly
537 identified within the longer convective envelope of the MJO.

538

539 *Daily atmospheric moisture budget*

540 Some theories of the MJO depend sensitively on the distribution and feedback of moisture
541 sources to the atmospheric column. We investigate whether the evaporation observed in
542 DYNAMO and TOGA COARE is significantly correlated to the precipitation, and whether
543 anomalous intraseasonal evaporation is a significant source of moisture to balance the
544 observed precipitation. We find weak but statistically significant correlations of evaporation
545 to precipitation (0.27 in TOGA COARE and 0.35 in DYNAMO, Figure 8). The daily
546 precipitation has a standard deviation of 290 W m^{-2} in latent heat units, much more than the
547 34 W m^{-2} standard deviation of evaporation. In situ observations show surface evaporation
548 anomalies in the tropical warm pool positively contribute to the MJO precipitation, but it has
549 a magnitude insufficient for generating and sustaining the precipitation associated with the
550 MJO. Even if they were highly correlated, the evaporation anomalies would explain only
551 $\sim 10\%$ of the variability of the precipitation.

552

553 The remaining $>90\%$ of the moisture must be supplied to precipitation by another source.

554 The budget for the integrated water in the atmospheric column is

$$0 = \underbrace{-\frac{\partial}{\partial t} \frac{1}{g} \int_0^{p_s} q_{tot} dp}_{\text{storage}} - \underbrace{\nabla \cdot F_q}_{\text{convergence}} + \underbrace{E}_{\text{evaporation}} - \underbrace{P}_{\text{precipitation}} \quad (1)$$

555 The first term is the column moisture storage. The budget is written so that all four terms sum
556 to zero, so negative storage means the column-integrated water is increasing. Moisture enters
557 the column through vertically integrated horizontal moisture flux convergence and surface

558 evaporation, and leaves by precipitation. The intraseasonal variation of our moisture flux
559 convergence computed as a residual from the moisture budget over the ship agrees with the
560 column integrated moisture flux convergence from the northern sounding array (Johnson et al.
561 2014). Estimates from the TOGA COARE and DYNAMO radiosonde arrays indicate most of
562 the precipitating water is supplied by moisture flux convergence (Lin and Johnson 1996;
563 Johnson and Ciesielski 2013).

564

565 We independently retrieve the column integrated water using the microwave radiometer on
566 the *Revelle* (Figure 9a). From the integrated column moisture we estimate the storage, and
567 then the convergence as a residual (Figure 9b). The column integrated moisture was variable
568 from day-to-day, but systematically reached a maximum in each of the convective phases of
569 the MJO. The intraseasonal range of integrated moisture during DYNAMO was about 2-3 cm,
570 on a background of 5-6 cm. The anomalous storage of 2-3 cm would be consumed in about a
571 day by a rain rate of 1 mm h^{-1} . Most daily rain rates were much less than 1 mm h^{-1} , yet four
572 days of very strong rain (2011 October 28, 30, November 24, and December 18) exceed 1
573 mm h^{-1} in the daily average, and 13 days (18% of the 71 local days sampled by the radar)
574 exceed 0.5 mm h^{-1} .

575

576 Daily precipitation in convective events easily exceeded the column supply of water, so the
577 storage of water vapor seems to play a relatively passive role compared to other terms in the
578 column water budget. From October 11-26, when the water vapor increased prior to
579 convective maximum II, the storage was variable but averaged -20 W m^{-2} , compared to
580 convergence of 140 W m^{-2} , evaporation of 100 W m^{-2} , and rain of 210 W m^{-2} . The column-
581 integrated water vapor sometimes took on larger values, therefore its intraseasonal variation
582 was not limited by being close to saturation.

583

584 Moisture flux convergence was usually on the order of the precipitation. It weakly exported
585 moisture from the column between convective events (October 5-9, November 12-18,
586 December 25-29). Moisture flux convergence imported moisture, approximately balancing
587 intermittent showers, in the several days before the convective maxima. This is in contrast to
588 the beginning of the convective maxima, when moisture flux convergence of 1500-3000 W
589 m^{-2} was balanced by rain and increases in column moisture storage. Total column water
590 increased despite the strong rain.

591

592 On November 28 there was positive storage (depletion of water) in the second Kelvin wave
593 of I2. We cannot sample all the terms in the budget over the complete convective lifetimes of
594 events I1 and I3, but storage became positive later in I1 on October 30, and was positive at
595 the end of I3 (beginning of leg 4) on December 19, suggesting column water anomalies
596 decreased toward the end of intraseasonal convective events. With a mean and standard
597 deviation of $110 \pm 30 \text{ W m}^{-2}$, evaporation is moderate and very constant compared to
598 fluctuations in rain ($210 \pm 290 \text{ W m}^{-2}$), storage (zero in the mean, but $-30 \pm 300 \text{ W m}^{-2}$ over
599 the three *Revelle* legs), and moisture flux convergence ($110 \pm 460 \text{ W m}^{-2}$).

600

601

602 *Intraseasonal air-sea interaction composites*

603 The DYNAMO and TOGA COARE experiments each were able to sample several
604 intraseasonal convective events. Now we place the events observed in DYNAMO and TOGA
605 COARE in the context of typical intraseasonal events from global data sets. A composite
606 average of a large number of events retains systematic intraseasonal variability, and removes

607 random variability that only affects individual events. Global data sets also show the zonal-
608 time evolution of intraseasonal convective events from the Indian Ocean to the Pacific Ocean,
609 including the DYNAMO and the TOGA COARE locations. The gridded data extend the
610 temporal and spatial sampling beyond the experiments, and allows comparison between
611 station observations of MJO structure to larger reanalysis-based MJO structures. The analysis
612 determines whether there are robust differences between intraseasonal variability observed in
613 the central Indian Ocean compared to the western Pacific Ocean.

614

615 Based on the principal component analysis, 103 intraseasonal events satisfied a criterion of
616 strong amplitude and eastward propagation (Appendix B). We composite the full unfiltered
617 anomalies of TropFlux gridded analysis surface flux variables during these events on the
618 phase of the MJO described by the leading two modes of principal component analysis of
619 OLR. Figure 10 shows the composite of the 103 events. The cycle before and the cycle after
620 the center of the event, when the MJO attains a convective maximum near 80°E, are each
621 divided into 24 phase bins. Daily data within ± 60 days of the center of the event are
622 composited according to their intraseasonal phase. The compositing procedure is described
623 further in Appendix B. Black contours in each panel show the negative OLR anomaly of the
624 first two principal components.

625

626 Color-shaded contours show the 103-event composite of OLR, SST, and surface fluxes. The
627 two PCs explain 37% of the intraseasonal OLR variance, so the composite OLR (Figure 10a)
628 recovers nearly the same pattern as the first two PCs of OLR used to construct the composite.
629 The minimum unfiltered OLR composite (shaded) slightly leads the PC-OLR regression
630 (contoured, Figure 10a). Convective events rapidly develop their minimum OLR with a quick
631 onset, and then slowly recover. Intraseasonal filtering and regression slows the apparent onset

632 and shifts the minimum OLR later relative to the unfiltered composite. The composite SST
633 and surface fluxes also have alternating eastward-propagating anomalies. Sea surface
634 temperature and SST tendency (Figure 10b and c) show SST cooling during the convective
635 phase of the events, which is consistent with the cooling by the net surface heat flux during
636 the convective phase of the MJO.

637

638 The amplitude and relative phase relation among the OLR, wind stress, SST, and each of the
639 components of the surface heat flux is relatively consistent across the warm pool from the
640 central Indian Ocean to the western Pacific Ocean. The net surface heat flux is synchronous
641 with OLR anomalies. Each of the components of the net surface heat flux is phased slightly
642 differently, yet the relative phase among the components is consistent throughout the warm
643 pool. The largest surface heat flux term, and that with the greatest intraseasonal composite
644 amplitude (25 W m^{-2}) is the solar radiation absorbed by the ocean in phase with high OLR.
645 (The surface solar radiation in gridded data sets is not independent of OLR. ISCCP uses OLR
646 retrievals to constrain the surface radiation, and after 2007 TropFlux surface solar radiation is
647 parameterized as a regression on OLR.) Some 3 W m^{-2} of the solar radiation is offset by
648 longwave radiation anomalies, though the longwave anomalies lead the OLR by less than a
649 quarter phase, perhaps indicating warm moist anomalies and emissive clouds in the lower
650 troposphere before the intraseasonal maximum of deep convective clouds.

651

652 Eastward wind stress is nearly synchronous with the OLR anomalies, so strong zonal
653 convergence accompanies the front (eastern) edge of the convective anomalies from 70°E to
654 the dateline. Sensible heat flux ($\pm 2 \text{ W m}^{-2}$, 25% of its mean) out of the ocean slightly leads,
655 while latent heat flux ($\pm 10 \text{ W m}^{-2}$, 10% of its mean) slightly follows the low OLR anomaly.
656 The phase of the surface heat fluxes can be explained by their factors: the friction velocity

657 scale $u^*=(|\tau|/\rho)^{1/2}$ and turbulent temperature scale T^* for sensible heat flux, or turbulent
658 humidity scale q^* for latent heat flux. Figure 11 shows the eastward wind stress (and hence
659 u^*) maximum slightly follows the peak of convection. Anticorrelation of intraseasonal q^*
660 with wind stress anomalies weakens the intraseasonal amplitude of the latent heat flux.
661 Surface air temperature is cooled by convection, enhancing sensible heat flux at the leading
662 edge of the convective anomaly.

663

664 The anomalies of OLR, SST, and surface heat fluxes become weaker over the Pacific Ocean
665 east of 170°E where climatological SST decreases below 29°C (Figure 11). Zonal wind
666 anomalies remain strong, however. The mean background wind reverses sign around 155°E
667 (Figure 2b) changing the configuration of intraseasonal surface heat flux anomalies relative
668 to wind stress over the eastern Pacific Ocean. The phase velocity increases considerably as
669 the convective MJO transitions to a dry Kelvin wave.

670

671

672 **5. Discussion**

673

674 Gridded flux products based on reanalyses (OAFflux and TropFlux) agree well with
675 DYNAMO observations from the *Revelle* at 0°N, 80.5°E, and with TOGA COARE
676 observations from the *Moana Wave* at 1.7°S, 156°E. The NCEP and ERA-I reanalyses both
677 ingest data from RAMA/TAO buoys. The nearest RAMA buoy is within 5 km of the *Revelle*
678 station in DYNAMO, and the TAO buoy at 156°E, 2°S is within 50 km of the *Moana Wave*,
679 which may have improved the performance of the reanalysis-based surface flux products
680 there, compared to locations far from any observations.

681

682 The evolution of intraseasonal convective and air-sea interaction anomalies (SST and surface
683 fluxes) was observed for 3 convectively active MJO events in the central Indian Ocean in
684 DYNAMO (2011-2012) and 3 MJO events in the western Pacific Ocean warm pool in TOGA
685 COARE (1992-1993). The results of the experiments showed slightly larger variations in
686 evaporation averaged over TOGA COARE (40 W m^{-2}) compared to DYNAMO (30 W m^{-2}).
687 The SST (29.1 ± 0.5 vs. 29.2 ± 0.4 °C) and latent heat fluxes (both 110 W m^{-2}) were
688 indistinguishable between the two experiments. The stronger latent heat flux variability in
689 TOGA COARE could be due to the growth of MJO anomalies as they propagate eastward,
690 larger ocean heat capacity in the western Pacific, or it could be due simply to sampling
691 different local realizations of 6 unique individual events.

692

693 Are these two handfuls of intensely observed MJO realizations representative of a typical
694 MJO? The composite of 103 MJO event anomalies in Figure 10 grows in amplitude in the
695 central Indian Ocean, reaching its maximum amplitude around 80°E , which corresponds to
696 the location of the DYNAMO field campaign. The MJO maintains nearly constant amplitude,
697 with a slight dip over the Maritime Continent, until it reaches about 160°E . The intraseasonal
698 composite OLR amplitude is slightly weaker over 155°E than over 80°E . The stronger events
699 observed during TOGA COARE were stronger for their own individual reasons, rather than a
700 systematic longitude dependence of typical MJO events. The 103 convective events in the
701 composite were chosen for their persistent amplitude and eastward propagation. It is possible
702 that some less persistent intraseasonal convective events do not propagate eastward
703 significantly, but have strong local signatures over the central Indian Ocean or western
704 Pacific Ocean.

705

706 Air-sea interaction observed in DYNAMO and TOGA COARE results from a variety of
707 atmospheric (and oceanic) waves embedded within the intraseasonal variability. There is
708 considerable synoptic atmospheric variability in the DYNAMO and TOGA COARE station
709 time series. Some of the convective disturbances observed in the TOGA COARE and
710 DYNAMO field experiments were related to the MJO, and others were not. The onset of two
711 convectively coupled Kelvin waves passing over the ship within the intraseasonal convective
712 maximum I2 in late November 2011 is an important and well-observed example of oceanic
713 and atmospheric processes within the MJO (Moum et al. 2014). On the other hand, the strong
714 synoptic variability in the wind stress, rain, and fluxes observed in TOGA COARE in
715 February 1993 project little onto intraseasonal time scales.

716

717 East of 80°E, zonal wind stress is steady and easterly for most of the suppressed phase and
718 for the beginning of the convective onset as composite OLR anomalies become more
719 negative than -5 W m^{-2} . Wind stress rapidly becomes eastward, reaching its maximum $\sim 1/16$
720 of a period after the time of minimum OLR. The wind stress relaxes gradually following the
721 maximum and flattens out in the suppressed phase. Hendon and Glick (1997) show the
722 eastward wind burst and evaporation maximum lagging the convection by ~ 1 week (more
723 than $1/8$ phase) behind the convection in the warm pool. The difference between their result
724 and ours could be explained by our compositing of the unfiltered anomalies on the phase of
725 the intraseasonal anomaly, compared to their time-lagged regression against a narrower (30-
726 90 day) band of intraseasonal OLR (e.g. their Fig. 11). Spectral truncation of the sharp rise
727 and slow relaxation of the wind in our composite will shift the eastward wind maximum later.

728

729 Lag regressions in the Indian Ocean (Hendon and Glick 1997, Woolnough et al. 2000) show
730 the timing of the wind stress even later and farther westward of the surface convection. In

731 DYNAMO wind stress rose sharply to a maximum within a few days of the maximum
732 convection. The nearly synchronous phase relation of wind stress and fluxes with convection
733 agrees with the phase relations found by Zhang and McPhaden (2000, their section 3c) from
734 their analysis of TAO buoy observations in the tropical western Pacific warm pool. The
735 phase of the zonal wind stress, heat flux, and SST to OLR is constant from 80° to 160°E in
736 our composite intraseasonal event.

737

738 Few research cruises venture to the poorly observed waters west of 70°E longitude due to the
739 danger of piracy. According to the reanalysis-based flux composites, the phase relation of the
740 zonal wind stress, net heat flux, and SST is different 40-70°E longitude, and it is over this
741 region that MJO OLR anomalies grow. Here eastward wind stress, surface heat flux, and cool
742 SST develop uniformly with longitude across 50-80°E after a negative OLR anomaly has
743 propagated eastward and intensified to a maximum at 70°E (Figure 11). The zonally uniform
744 wind stress west of 70°E then propagates with OLR from 80-160°E. In the western Indian
745 Ocean SST responds more strongly to intraseasonal surface fluxes than the central and
746 eastern Indian Ocean. Its response to the net surface heat flux is twice as large at 50°E as it is
747 east of 80°E.

748

749 The eastward wind stress in the western Indian Ocean is consistent with frictional flow
750 towards low surface pressure induced under the convective heating anomaly growing to the
751 east. The cool SST anomaly in the western Indian Ocean reinforces the pressure gradient
752 pushing the eastward wind anomaly. The phase of the wind anomaly at 50°E is consistent
753 with the convergence in Hendon and Salby (1994, their Fig. 8c) and the latent heat flux in
754 Hendon and Glick (1997). The timing of wind stress to convection in the central Indian
755 Ocean is the same as farther east, yet it is possible that the climatological western Indian

756 Ocean SST gradient and the long fetch of eastward wind stress collects moisture evaporated
757 over a large area extending ~2000 km to the west, and thereby amplifies convective
758 anomalies in the central Indian Ocean.

759

760 Surface evaporation is the process through which most of the solar energy absorbed by the
761 ocean enters the atmosphere. In moisture mode quasi-equilibrium theories of the MJO,
762 evaporation anomalies are proposed as a means of increasing the column moist static energy
763 in the convective region in order to grow the convective anomaly (e.g. Maloney and Sobel
764 2004, Sugiyama et al. 2009). In TOGA COARE (Lin and Johnson 1996) and DYNAMO
765 (Figure 9 and Figure 12) observations, local mean evaporation is less than 1/2 of the mean
766 precipitation. Evaporation is moderate and steady compared to fluctuations of the
767 precipitation and horizontal moisture flux convergence. Daily average evaporation increases
768 40% in westerly wind bursts, while daily precipitation maxima are an order of magnitude
769 greater. Evaporation moistens the boundary layer slowly, so boundary layer moisture
770 convergence must fetch moisture from a large area to explain the maxima in precipitation.
771 We refer to *moisture fetch* as both the large area of the atmospheric boundary layer
772 moistened by surface evaporation, and the process by which the large-scale circulation
773 fetches moisture over this large area to feed the convection. The challenge for MJO theories
774 then is to explain by what process relatively uniform evaporation and boundary layer
775 moisture converges into the region of convection.

776

777 Maloney (2009) found advection of moisture and surface evaporation contributed in similar
778 magnitude to lower tropospheric moist static energy anomalies, but evaporation opposes the
779 recharge of moist static energy in the suppressed phase. While SST anomalies have only a
780 small effect on the fluxes, it is possible that positive SST anomalies over a large area in

781 advance and east of convection can induce a broad area of low surface pressure and large-
782 scale frictional convergence (e.g. Lindzen and Nigam 1989, Back and Bretherton 2009). This
783 boundary layer convergence would fetch moisture from a wide area of the planetary
784 boundary layer, having average surface evaporation, toward convectively coupled
785 precipitating atmospheric waves. DeMott et al. (2014) described enhancement of the MJO by
786 systematic moisture convergence over warm SST east of the convection in atmosphere-ocean
787 coupled general circulation models.

788

789 Frictional boundary layer convergence on the equator east of the convective maximum has
790 been found to destabilize the atmosphere to convection (Rui and Wang 1990, Maloney and
791 Hartmann 1998). Maloney and Kiehl (2002) observed that intraseasonal SST anomalies in
792 the eastern tropical Pacific Ocean also induced surface convergence. The result of a quasi-
793 equilibrium model would be enlightening were it to explicitly include boundary layer
794 convergence due to intraseasonal SST anomalies. The boundary layer adjustment to SST
795 anomalies is a potential source of instability for intraseasonal convective anomalies, even if
796 there are only weak temperature gradients in the free troposphere. The role of nonlinear
797 moisture advection was key to eastward-propagating anomalies in the Sobel and Maloney
798 (2012) quasi-equilibrium model. The effect of intraseasonal SST anomalies on it could also
799 be assessed.

800

801

802 **6. Conclusion**

803

804 DYNAMO, TOGA COARE, and gridded flux analysis composites have wind stress,
805 convergence, and heat fluxes nearly in phase with convection from 70-160°E, consistent with

806 previous findings from in situ observations in the warm pool (Zhang and McPhaden 2000).
807 Eastward wind stress increases rapidly in the convective phase as wind converges slightly
808 before (east of) the minimum OLR anomaly. Net heat flux anomalies are nearly in phase with
809 the convection indicated by low OLR, with sensible heat flux strongest at the onset of
810 convection, and wind stress and latent heat flux increasing as the convective phase matures.
811 Convection, wind stress, and other related variables have a rapid onset followed by a slow
812 recovery. Intraseasonal filtering of these variables' asymmetrical temporal structure
813 introduces phase delays.

814

815 In TOGA COARE, DYNAMO, and the gridded flux products, net surface fluxes out of the
816 ocean increase during the convective phase of the MJO, mostly from enhanced evaporation
817 due to stronger wind and decreased solar radiation due to clouds. Surface turbulent fluxes are
818 relatively steady over intraseasonal time scales, with composite cycles in gridded flux
819 analyses with ranges of only $\pm 2 \text{ W m}^{-2}$ (25%) for sensible heat flux and $\pm 10 \text{ W m}^{-2}$ (9%) for
820 latent heat flux (Figure 10). Daily flux anomalies 3 times larger than the gridded analyses
821 were observed in DYNAMO, roughly consistent with the larger daily OLR and SST
822 anomalies than their intraseasonal regression time series (Figure 4).

823

824 The observations help us assess the contribution to the MJO of three conceptual models of
825 atmosphere-ocean interaction: surface flux feedback, coupled ocean-atmosphere interaction,
826 and atmospheric moisture recharge. The phase of surface fluxes to the MJO convective
827 anomaly suggests that intraseasonal surface fluxes increase moist static energy during MJO
828 convection, contributing a positive feedback. The surface evaporation increases 30-50%
829 relative to its mean during the convective phase, yet this anomaly constitutes less than 10%
830 of the moisture required for the precipitation (Figure 12). The magnitude of the anomalous

831 surface flux is only a small contributor to the moisture (or moist static energy) budget, but
832 moisture mode theories do not require significant local evaporation anomalies for
833 precipitation. For strongly negative gross moist stability only a small amount of evaporation
834 is needed to destabilize the column to generate precipitation and moisture convergence. In
835 these models evaporation does not drive precipitation directly through recharging the
836 available water budget, but by destabilizing and increasing the moist static energy of the
837 column that then induces large-scale moisture flux convergence.

838

839 Intraseasonal SST anomalies suggest coupled ocean-atmosphere variability also amplifies the
840 MJO. The SST and ocean mixed layer temperature responds to the intraseasonal variability of
841 the fluxes. SST increases during the suppressed phase, reaching a maximum at the onset of
842 convection. Mixed layer ocean temperature (measured at night or at 10 m depth) has an
843 intraseasonal range of 1-2 °C in TOGA COARE and DYNAMO. The intraseasonal
844 composite SST has a range of only about 0.2-0.3 °C, similar to Hendon and Glick (1997)
845 Figure 11, Zhang and McPhaden (2000) Figure 11, and Benedict and Randall (2007) Figure
846 4c. We cannot completely explain this striking difference between SST time series from the
847 field experiments and the analyses. The ocean temperature response to the MJO events
848 observed in TOGA COARE and DYNAMO appear to have been stronger than average.

849

850 Most satellite SST products avoid sampling during the day, so the effect of the diurnal warm
851 layer is nearly absent from the gridded products. Calm wind and strong solar flux raise the
852 SST in the suppressed intraseasonal phase, as measured at 0.1 m in DYNAMO and TOGA
853 COARE (Marion, 2014). Diurnal SST warming occurs when winds and turbulent fluxes are
854 weak, thus it reduces intraseasonal variability of surface fluxes (de Szoeke and Edson 2014).
855 The diurnal warm layer makes the maximum SST occur a few days earlier than the mixed

856 layer temperature, which could contribute to the MJO by enhancing heat fluxes and frictional
857 convergence ahead of the convective phase.

858

859 The moisture recharge conceptual model depends on moisture building up in the atmosphere
860 in advance of the convective phase of the MJO. In an analysis of tropical soundings and
861 reanalysis, Kemball-Cook and Weare (2001) found a moisture increase and convergence
862 ($-\nabla \cdot \mathbf{u}$) ahead of convection for equatorial locations. Their analysis and the DYNAMO
863 *Revelle* equatorial time series support the frictional wave-CISK theory in which frictional
864 boundary layer convergence destabilizes convective waves within a narrow band near the
865 equator. Off the equator, they found convergence was synchronous with convection rather
866 than with increasing moisture. Though horizontal convergence is not equivalent to moisture
867 advection, the lack of convergence off the equator led Kemball-Cook and Weare (2001) to
868 propose that moisture recharge by local evaporation there preconditioned the atmosphere for
869 deep convection.

870

871 While there is local evaporation, the processes responsible for moistening are very unlikely to
872 be purely local, on or off the equator. Observations show evaporation is relatively constant at
873 about half the mean precipitation over the warm equatorial regions of the Indian and Pacific
874 Oceans. Thus on the whole, moisture must converge horizontally into the region. Synoptic
875 convectively-coupled Kelvin and Rossby waves comprise intense convective rain events
876 within the MJO in DYNAMO and TOGA COARE. The days of strongest rain exceed
877 evaporation by an order of magnitude and yield an increase in integrated column moisture
878 (Figure 9). This implies that anomalous column moisture flux convergence is important for
879 the MJO and its embedded convective storms. The moisture budget does not distinguish

880 whether the moisture convergence is the cause or the consequence of precipitating synoptic
881 storms. Even if the moisture convergence is not the cause of precipitation, the similar
882 magnitude of synoptic convergence and precipitation still suggests that the aggregate of
883 precipitation from storms is related to convergence in the MJO. The requirement for moisture
884 convergence to balance the local moisture budget on daily and long-term mean time scales
885 leads us to expect that moisture convergence is important to supply moisture to precipitation
886 in the MJO convective phase. The moisture contributed steadily by evaporation is absolutely
887 critical to the tropical circulation, the MJO, and the convective storms. The accumulation of
888 moisture over time and the convergence of moisture over space determine exactly when,
889 where, and how much it rains.

890

891 With only 3 intraseasonal realizations from the ship in DYNAMO, we cannot clearly
892 distinguish intraseasonal recharge from synoptic discharge of moisture anomalies. The
893 increase of column moisture during the inactive phase supports the recharge mechanism for
894 MJO convection, but the same magnitude increase of moisture during the strongest
895 precipitation suggests the interaction of convection with the column moisture is more
896 complicated than the simple moisture recharge paradigm.

897

898 DYNAMO sampled the MJO in the central Indian Ocean at the completion of its early
899 genesis phase and the beginning of its mature phase where intraseasonal OLR and surface
900 flux variables reach their maximum amplitude. Air-sea interaction may be different in the
901 earlier genesis of the MJO in the western Indian Ocean, where intraseasonal SST responds
902 more sensitively to the net surface flux. The large region of enhanced westerly wind and
903 evaporation anomalies in the western Indian Ocean may contribute to the MJO when it is
904 growing in central Indian Ocean.

905

906 **Acknowledgement**

907 We would like to thank the three anonymous reviewers. Their helpful and timely reviews
908 significantly improved this work. We thank Sergio Pezoa, Kenneth Moran, Daniel Wolfe,
909 Raymond Kreth, Sasha Perlin, and the crew of the R/V *Revelle*, without whom collecting
910 these observations would not have been possible. TOGA COARE Air-Sea Fluxes and Sea-
911 Surface Data are provided by the Research Data Archive at the National Center for
912 Atmospheric Research, Computational and Information Systems Laboratory.
913 <http://rda.ucar.edu/datasets/ds606.1/>. Interpolated OLR data are provided by the
914 NOAA/OAR/ESRL PSD, Boulder, Colorado, USA, from their Web site at
915 <http://www.esrl.noaa.gov/psd/>. OAFflux data are graciously provided by Woods Hole
916 Oceanographic Institution at <http://oafux.whoi.edu/>. The TropFlux data is produced under
917 a collaboration between Laboratoire d'Océanographie: Expérimentation et Approches
918 Numériques (LOCEAN) from Institut Pierre Simon Laplace (IPSL, Paris, France) and
919 National Institute of Oceanography/CSIR (NIO, Goa, India), and supported by Institut de
920 Recherche pour le Développement (IRD, France). ISCCP FD data are available from
921 <http://isccp.giss.nasa.gov/projects/flux.html>. We gratefully acknowledge support from
922 NOAA OAR grants NA11OAR4310076 and NA13OAR4310160, and ONR grants N00014-
923 10-1-0299, N00014-10-1-0546, and N00014-14-1-0140.

924

925

926 **Appendix A: Description of the DYNAMO data**

927

928 In situ meteorology and high-rate flux sensors operated continuously during the 4 legs of the
929 DYNAMO experiment. Continuous 1- and 10-minute resolution time series of
930 meteorological means, fluxes, related measurements, and derived data, from the *Revelle*
931 DYNAMO research cruises are available at <ftp://dynamo.dms.uconn.edu/>, and linked from
932 the DYNAMO field catalog <http://catalog.eol.ucar.edu/dynamo/>. Data were sampled at the
933 frequencies and heights specified in Table A1 and variables are adjusted to standard heights
934 of 2 or 10 m using Monin-Obukhov similarity accounting for hydrostatic pressure and
935 adiabatic temperature changes.

936

937 *Wind Speed*

938 Velocity is measured by 3 sonic anemometers deployed on the forward mast by NOAA Earth
939 Systems Research Laboratory/Physical Sciences Division (ESRL/PSD), UConn and OSU.
940 The wind speeds are averaged from the sensor(s) best exposed to the wind, depending on the
941 relative wind direction. Aside from buoy deployment activities during leg 1, the *Revelle* was
942 usually positioned with the bow pointing into the mean current to allow oceanic
943 microstructure profiling from the fantail, providing relative wind directions within $\pm 90^\circ$ of
944 the bow for 81% of the time and $\pm 135^\circ$ of the bow for 93% of the time. Winds were excluded
945 from relative wind directions outside $\pm 135^\circ$. The winds are corrected for flow distortion
946 using an empirical correction based on comparisons with nearby buoys and LIDAR derived
947 winds.

948

949 *Temperature, Pressure and Humidity*

950 Two aspirated temperature/relative humidity sensors on the bow mast measured air
951 temperature and humidity (T/RH). T/RH measurements are processed to remove heat

952 contamination of the ship during daylight. We post-calibrated the T/RH sensors in either a
953 calibration chamber at UConn, or at the manufacturer (Vaisala); both calibrations agree. The
954 ESRL/PSD temperature sensor had the most effective aspirator and the least contamination
955 by solar heating. In one period its fan failed and the aspirated UConn temperature sensor was
956 used. Specific humidity and air pressure are computed from the aspirated UConn T/RH and
957 pressure sensors. Specific humidity is less sensitive to solar heating as long as the
958 temperature and RH are measured simultaneously. RH is then reconstructed from the
959 specific humidity, pressure and the best estimate of the air temperature.

960

961 *Sea Temperature, Salinity, and Currents*

962 Near surface sea temperature was measured by the “sea-snake” comprised of a towed
963 thermistor floating approximately 5 cm beneath the surface. The sea-snake measurements
964 are reduced by 0.058°C based on a comparison with a sub-surface temperature chain
965 deployed by OSU ocean mixing group as described in Moum et al. (2014). The water
966 interface temperature is computed from the sea-snake adjusted for the effects of the viscous
967 cool skin (Saunders 1967, Fairall et al. 1996b). Sea surface temperatures were additionally
968 estimated by radiometric measurements of skin temperature (Chris Zappa, Lamont Doherty
969 Earth Observatory). These SST estimates filled gaps during the first 11 days of leg 2 when
970 problems were encountered with the sea-snake measurements. Values of the temperature and
971 salinity are also measured at approximately 4.9 m depth by the ship’s intake
972 thermosalinograph. Surface currents were collected from the ship’s ADCP and quality
973 control by the OSU ocean mixing group (Moum et al. 2014).

974

975 *Precipitation*

976 Precipitation was provided by the ESRL/PSD optical rain gauge located on the forward mast
977 after calibration with 5 catchment rain gauges deployed by OSU, UConn and the
978 meteorological sensors of the *Revelle*. All catchment rain gauges were in good agreement
979 during periods of low winds. The optical rain gauge was correlated well, but was adjusted by
980 a factor of 1.4 to agree with the mean rain rate of the other gauges. During periods of high
981 winds, the manual and self-siphoning rain gauges appeared to underestimate the daily
982 precipitation compared to the adjusted optical rain gauge. Presumably, this is due to the
983 effect of flow distortion on the rain gauges. The optical rain had good exposure on the
984 forward mast and lower sensitivity to wind. Therefore, the adjusted rain rate from the optical
985 rain gauge is used as the in situ time series of precipitation from the *Revelle*. The adjusted
986 rain rate from the optical rain gauge agrees well with nearby buoy measurements.

987

988 *Radiative Fluxes*

989 The downwelling thermal infrared (IR) radiation is computed using an average of the motion-
990 stabilized ESRL/PSD pyrgeometers mounted above the O2 deck and the ship's pyrgeometer
991 on the top of the forward mast. The pyrgeometers are corrected for the effects of solar
992 heating. The upwelling IR radiation is modeled from the SST computed from the sea-snake,
993 accounting for emission and reflection using an emissivity, $\varepsilon = 0.97$. Downwelling solar
994 radiation is measured by the ship's pyranometer on the top of the forward mast. The
995 upwelling solar radiation is computed from a commonly used parameterization for surface
996 albedo of the ocean as a function of solar altitude (Payne1972).

997

998 Measurements of the diffuse solar radiation are made by a National Center for Atmospheric
999 Research (NCAR) SPN1 sunshine pyranometer deployed on the top of the forward mast.

1000 Clear sky solar radiation (i.e. and atmosphere with no clouds) is estimated by a model
1001 adapted from Iqbal (1988) for total solar irradiance (1367 W m^{-2}), solar zenith angle, and
1002 absorption and scattering by gases, aerosols, ozone, and water vapor; and tuned to match
1003 observations on clear days.

1004

1005 *Surface Fluxes of Heat, Mass and Momentum*

1006 The optimized set of mean meteorological and surface ocean measurements (wind,
1007 temperature, currents) are used to compute the latent, sensible, and rain fluxes with the
1008 COARE 3.5 algorithm (Fairall et al. 1996, Fairall et al. 2003, Edson et al. 2013), using the
1009 wind speed relative to the ocean surface. The transfer coefficients in COARE 3.5 have been
1010 adjusted to match the heat fluxes given by COARE 3.0. Continued improvement and
1011 validation of the COARE algorithm is a goal of the experiment, and ESRL/PSD, UConn, and
1012 OSU deployed turbulence flux instrumentation (sonic anemometers and infrared gas
1013 analyzers) to compute fluxes with the eddy correlation method.

1014

1015 *Atmospheric Remote Sensing*

1016 In addition to the flux system there were 3 upward-looking remote systems operated by
1017 ESRL/PSD: A mechanically stabilized W-Band Doppler cloud radar (Moran et al. 2012), a
1018 2-channel (23 and 31 GHz) microwave radiometer, and a lidar ceilometer. The W-band
1019 cloud radar sampled clouds and precipitation in low-altitude mode (0-7 km) when on station
1020 at the equator, and in high-altitude mode (0-14 km) when the *Revelle* was in transit. The
1021 microwave radiometer sampled column liquid water and water vapor path, and the
1022 ceilometers sampled cloud base heights and uncalibrated optical backscatter. These remote
1023 sensing measurements have been analyzed to retrieve hourly cloud properties such as cloud
1024 liquid water concentration, cloud top height, and cloud base height. These values are

1025 available at
1026 ftp://ftp1.esrl.noaa.gov/psd3/cruises/DYNAMO_2011/Revelle/radar/wband/processed/

1027

1028 *Surface Wave Measurements*

1029 A laser altimeter was pointed forward of the forward mast to provide measurements of the
1030 surface wave field during DYNAMO legs 2-4. It provides hourly estimates of the significant
1031 wave height and phase speed of the dominant waves from the frequency at the spectral peak
1032 between 0.01 and 0.5 Hz.

1033

1034 **Appendix B**

1035

1036 *Principal component analysis procedure*

1037 We use a PCA method to decompose the intraseasonally filtered time-longitude structure of
1038 OLR into an efficient representation of the MJO, and to find the surface flux expression of
1039 the MJO. The PCA is quite standard and similar to that used by others to describe the MJO
1040 (e.g. Shinoda et al. 1998). Our unique event identification and compositing method relies on
1041 the PCA, so we briefly introduce the PCA here. The intraseasonally filtered time series-
1042 longitude matrix (e.g. of OLR) X_* can be written as a product using singular value
1043 decomposition:

1044

$$1045 \quad X_* = U \Sigma V^T = P_* F_* \quad (B1)$$

1046

1047 where the superscript T stands for the matrix transpose. Other numerical methods for the PCA
1048 (e.g. eigenvector decomposition of the covariance matrix) are equivalent. The columns of

1049 $P_*=N^{1/2}U$ are the unity-variance normalized principal component time series. N is the number
1050 of samples (days). The rows of $F_*=N^{-1/2}\Sigma V^T$ are the empirical orthogonal functions of
1051 longitude. A row of F_* has the same units as X_* (e.g. $W m^{-2}$ for OLR) and represents the
1052 spatial pattern realized by a standard deviation of 1 in the corresponding PC time series.

1053

1054 We truncate the expansion P_* and F_* to the first two principal component time series $P=[P_1$
1055 $P_2]$ and the first two empirical orthogonal functions F . The truncated time-longitude series
1056 explained by the first two PCs is

1057

$$1058 \qquad \qquad \qquad X=PF. \qquad \qquad \qquad (B2)$$

1059

1060 In analogy to F , the spatial pattern G of another variable (e.g. surface flux) Y_* explained by
1061 the principal component can be generated by projection (regression) onto the truncated
1062 principal component P :

1063

$$1064 \qquad \qquad \qquad G=P^T Y_*. \qquad \qquad \qquad (B3)$$

1065

1066 Analogous to X , the truncated time-space variability of Y_* associated with the first two PCs
1067 and hence the MJO is

1068

$$1069 \qquad \qquad \qquad Y=PG=P(P^T Y). \qquad \qquad \qquad (B4)$$

1070

1071 *Event identification*

1072 Surface sea-air fluxes were composited in MJO events. MJO events were defined by the two-
 1073 dimensional state space of the first two normalized PC time series. The phase ϕ of the MJO at
 1074 time t is

1075

$$1076 \quad \phi = \tan^{-1}(P_2(t)/P_1(t)). \quad (B5)$$

1077

1078 the angle of the vector (P_1, P_2) of the leading two principal components. Shinoda et al. (1998)
 1079 defines MJO events according to PC amplitudes meeting thresholds and progressing eastward
 1080 ($P_1 < -1.5$ followed by $P_1 > 0$ and $P_2 < -1.5$ within 25 days). Some strong OLR anomalies,
 1081 including the DYNAMO convective events, did not meet these thresholds. We used another
 1082 criterion based on the integrated area swept out by the eastward-phase progression of PC1
 1083 and PC2 to identify MJO events. The area of a sector of (P_1, P_2) space swept out between
 1084 successive days is

$$1085 \quad (|P^2|/2) d\phi \quad (B6)$$

1086

1087 where $|P^2| = P_1^2 + P_2^2$ is the square of the magnitude of the vector (P_1, P_2) , and the phase angle
 1088 between successive days P^- and P^+ is

1089

$$1090 \quad d\phi = \tan^{-1}((P_1^- P_2^+ - P_2^- P_1^+) / (P_1^- P_1^+ + P_2^- P_2^+)). \quad (B7)$$

1091

1092 Positive $d\phi$ corresponds to eastward propagation of OLR anomalies.

1093

1094 MJO events are identified when the area of the sector swept out by the normalized vector in
 1095 (P_1, P_2) space over 25 days is greater than $\pi/2$. This area is equivalent to that of a semicircle
 1096 with a radius of one standard deviation. This condition identifies events that propagate

1097 eastward with significant amplitude. The condition identifies 103 events in the 27.5 years of
1098 OLR data analyzed.

1099

1100 *Compositing by intraseasonal phase*

1101 The phase depends on the arbitrary signs of P_1 and P_2 . For our P_1 and P_2 there are negative
1102 intraseasonal OLR anomalies over the central Indian Ocean when $P_1 < 0$ and $P_2 = 0$. If the
1103 centered 25-day integral satisfies the above criterion, the day that $P_1 < 0$ and $P_2 = 0$ is identified
1104 as day 0 ($\phi = 0$) of the event. The daily unfiltered 15°S - 15°N average OLR and surface
1105 variables within ± 60 days of day 0 are then composited on the phase of the OLR PC index.
1106 Daily data in the 60 days prior to day 0 are assigned to one of 24 phase bins corresponding to
1107 the cycle preceding day zero. Data in the 60 days following day zero are assigned to one of
1108 24 phase bins after event day zero. Days are not composited for a time difference of more
1109 than 60 days or for a phase difference more than 2π . In this way we composite two
1110 intraseasonal cycles for each event, one before and one after $\phi = 0$ when the maximum
1111 amplitude is obtained in the central Indian Ocean.

1112

1113 **References**

1114

1115 Anderson, S. P., R. A. Weller, and R. B. Lukas, 1996: Surface buoyancy forcing and the
1116 mixed layer of the western Pacific warm pool: Observations and 1D model results.
1117 *J. Climate*, **9**, 3056-3085, doi:10.1175/1520-
1118 0442(1996)009<3056:SBFATM>2.0.CO;2.

1119 Back, L. E., and C. S. Bretherton, 2009: On the relationship between SST gradients,
1120 boundary layer winds, and convergence over the tropical oceans. *J. Climate*, **22**,
1121 4182-4196, 10.1175/2009JCLI2392.1.

1122 Benedict, J. J., and D. A. Randall, 2009: Structure of the Madden-Julian Oscillation in the
1123 superparameterized CAM. *J. Atmos. Sci.*, **66**, 3277-3296.

1124 Benedict, J. J., and D. A. Randall, 2011: Impacts of idealized air–sea coupling on
1125 Madden–Julian Oscillation structure in the superparameterized CAM. *J. Atmos.*
1126 *Sci.*, **68**, 1990-2008, 10.1175/JAS-D-11-04.1.

1127 Benedict, J. J., E. D. Maloney, A. H. Sobel, and D. M. W. Frierson, 2014: Gross moist
1128 stability and MJO simulation skill in three full-physics GCMs. *J. Atmos. Sci.*, **71**,
1129 3327-3349, 10.1175/JAS-D-13-0240.1.

1130 Bladé, I., and D. L. Hartmann, 1993: Tropical intraseasonal oscillations in a simple
1131 nonlinear model. *J. Atmos. Sci.*, **50**, 2922-2939, 10.1175/1520-
1132 0469(1993)050<2922:TIOIAS>2.0.CO;2.

1133 Charnock, H., 1955: Wind stress on a water surface. *Quart. J. Roy. Met. Soc.*, **81**, 639-
1134 640, 10.1002/qj.49708135027.

1135 Dee, D. P., and Coauthors, 2011: The ERA-Interim reanalysis: configuration and

1136 performance of the data assimilation system. *Quart. J. Roy. Met. Soc.*, **137**, 553-
1137 597, 10.1002/qj.828.

1138 DeMott, C. A., C. Stan, D. A. Randall, and M. D. Branson, 2014: Intraseasonal
1139 variability in coupled GCMs: The roles of ocean feedbacks and model physics. *J.*
1140 *Climate*, 10.1175/JCLI-D-13-00760.1.

1141 de Szoeke, S. P., and J. B. Edson, 2014: Intraseasonal air-sea interaction and convection
1142 observed in DYNAMO/CINDY/AMIE. *The global monsoon system: research*
1143 *and forecast*, C. P. Chang, Ed., World Scientific.

1144 Donlon, C. J., M. Martin, J. Stark, J. Roberts-Jones, E. Fiedler, and W. Wimmer, 2012:
1145 The Operational Sea Surface Temperature and Sea Ice Analysis (OSTIA) system.
1146 *Remote Sensing of Environment*, **116**, 140-158,
1147 <http://dx.doi.org/10.1016/j.rse.2010.10.017>.

1148 Edson, J. B., A. A. Hinton, K. E. Prada, J. E. Hare, and C. W. Fairall, 1998: Direct
1149 covariance flux estimates from mobile platforms at sea. *J. Atmos. and Oceanic*
1150 *Tech.*, **15**, 547-562.

1151 Edson, J. B., and Coauthors, 2013: On the exchange of momentum over the open ocean. *J.*
1152 *Phys. Oceanogr.*, **43**, 1589-1610, 10.1175/JPO-D-12-0173.1.

1153 Emanuel, K. A., 1987: An Air-Sea Interaction Model of Intraseasonal Oscillations in the
1154 Tropics. *J. Atmos. Sci.*, **44**, 2324-2340, 10.1175/1520-
1155 0469(1987)044<2324:AASIMO>2.0.CO;2.

1156 Fairall, C. W., E. F. Bradley, D. P. Rogers, J. B. Edson, and G. S. Young, 1996a: Bulk
1157 parameterization of air-sea fluxes for Tropical Ocean-Global Atmosphere
1158 Coupled-Ocean Atmosphere Response Experiment. *J. Geophys. Res.*, **101**, 3747-

1159 3764.

1160 Fairall, C. W., E. F. Bradley, J. S. Godfrey, G. A. Wick, J. B. Edson, and G. S. Young,
1161 1996b: Cool-skin and warm-layer effects on sea surface temperature. *Journal of*
1162 *Geophysical Research: Oceans*, **101**, 1295-1308, 10.1029/95JC03190.

1163 Fairall, C. W., A. B. White, J. B. Edson, and J. E. Hare, 1997: Integrated shipboard
1164 measurements of the marine boundary layer. *J. Atmos. and Oceanic Tech.*, **14**,
1165 338-359.

1166 Fairall, C. W., E. F. Bradley, J. E. Hare, A. A. Grachev, and J. B. Edson, 2003: Bulk
1167 parameterization of air-sea fluxes: updates and verification for the COARE
1168 algorithm. *J. Climate*, **19**, 571-591.

1169 Feng, Z., S. Hagos, A. K. Rowe, C. D. Burleyson, M. N. Martini, and S. P. de Szoeke,
1170 2014: Mechanisms of convective cloud organization by cold pools over tropical
1171 warm ocean during the AMIE/DYNAMO field campaign. *J. Adv. Model. Earth*
1172 *Syst.* submitted.

1173 Flatau, M., P. J. Flatau, P. Phoebus, and P. P. Niiler, 1997: The feedback between
1174 equatorial convection and local radiative and evaporative processes: the
1175 implications for intraseasonal oscillations. *J. Atmos. Sci.*, **54**, 2373-2386,
1176 10.1175/1520-0469(1997)054<2373:TFBECA>2.0.CO;2.

1177 Gill, A. E., 1980: Some simple solutions for heat-induced tropical circulation. *Quart. J.*
1178 *Roy. Met. Soc.*, **106**, 447-462.

1179 Hannah, W. M., and E. D. Maloney, 2014: The moist static energy budget in NCAR
1180 CAM5 hindcasts during DYNAMO. *Journal of Advances in Modeling Earth*
1181 *Systems*.

1182 Harrison, D. E., and G. A. Vecchi, 2001: January 1999 Indian Ocean cooling event.
1183 *Geophys. Res. Lett.*, **28**, 3717-3720, 10.1029/2001gl013506.

1184 Hendon, H. H., and J. Glick, 1997: Intraseasonal air-sea interaction in the tropical Indian
1185 and Pacific Oceans. *J. Climate*, **10**, 647-661, 10.1175/1520-
1186 0442(1997)010<0647:IASIIT>2.0.CO;2.

1187 Hendon, H. H., 2005: Air-sea interaction. *Intraseasonal Variability in the Atmosphere-
1188 Ocean Climate System*, W. K. M. Lau, and D. E. Waliser, Eds., Praxis, Springer,
1189 223-246.

1190 Iqbal, M., 1988: Spectral and total sun radiance under cloudless skies. *Physical
1191 Climatology for Solar and Wind Energy*, R. Guzzi, and C. G. Justus, Eds., World
1192 Scientific, 196–242.

1193 Inness, P. M., and J. M. Slingo, 2003: Simulation of the Madden–Julian Oscillation in a
1194 coupled general circulation model. Part I: Comparison with observations and an
1195 atmosphere-only GCM. *J. Climate*, **16**, 345-364, 10.1175/1520-
1196 0442(2003)016<0345:SOTMJO>2.0.CO;2.

1197 Johnson, R. H., T. M. Rickenbach, S. A. Rutledge, P. E. Ciesielski, and W. H. Schubert,
1198 1999: Trimodal characteristics of tropical convection. *J. Climate*, **12**, 2397-2418.

1199 Johnson, R. H., and P. E. Ciesielski, 2013: Structure and properties of Madden–Julian
1200 Oscillations deduced from DYNAMO sounding arrays. *J. Atmos. Sci.*, **70**, 3157-
1201 3179, 10.1175/JAS-D-13-065.1.

1202 Kalnay, E., and Coauthors, 1996: The NCEP/NCAR 40-year reanalysis project. *Bull.
1203 Amer. Meteorol. Soc.*, **77**, 437-471, doi:10.1175/1520-
1204 0477(1996)077<0437:TNYRP>2.0.CO;2.

1205 Kanamitsu, M., W. Ebisuzaki, J. Woollen, S.-K. Yang, J. J. Hnilo, M. Fiorino, and G. L.
1206 Potter, 2002: NCEP–DOE AMIP-II reanalysis (R-2). *Bull. Amer. Meteorol. Soc.*,
1207 **83**, 1631-1643, 10.1175/BAMS-83-11-1631.

1208 Kemball-Cook, S. R., and B. C. Weare, 2001: The onset of convection in the Madden–
1209 Julian Oscillation. *J. Climate*, **14**, 780-793, 10.1175/1520-
1210 0442(2001)014<0780:TOOCIT>2.0.CO;2.

1211 Kiladis, G. N., M. C. Wheeler, P. T. Haertel, K. H. Straub, and P. E. Roundy, 2009:
1212 Convectively coupled equatorial waves. *Reviews of Geophysics*, **47**, RG2003,
1213 10.1029/2008RG000266.

1214 Kiladis, G. N., and Coauthors, 2014: A comparison of OLR and circulation-based indices
1215 for tracking the MJO. *Mon. Wea. Rev.*, **142**, 1697-1715, 10.1175/MWR-D-13-
1216 00301.1.

1217 Kim, D., and Coauthors, 2009: Application of MJO simulation diagnostics to climate
1218 models. *J. Climate*, **22**, 6413-6436, 10.1175/2009jcli3063.1.

1219 Krishnamurti, T. N., D. K. Oosterhof, and A. V. Mehta, 1988: Air-sea interaction on the
1220 time scale of 30 to 50 days. *J. Atmos. Sci.*, **45**, 1304-1322, 10.1175/1520-
1221 0469(1988)045<1304:AIOTTTS>2.0.CO;2.

1222 Lau, K.-M., and L. Peng, 1987: Origin of low-frequency (intraseasonal) oscillations in
1223 the tropical atmosphere. Part I: Basic theory. *J. Atmos. Sci.*, **44**, 950-972,
1224 doi:10.1175/1520-0469(1987)044<0950:OOLFOI>2.0.CO;2.

1225 Liebmann, B., and C. A. Smith, 1996: Description of a complete (interpolated) outgoing
1226 longwave radiation dataset. *Bull. Amer. Meteorol. Soc.*, **77**, 1275-1277.

1227 Lin, J., B. Mapes, M. Zhang, and M. Newman, 2004: Stratiform precipitation, vertical

1228 heating profiles, and the Madden–Julian Oscillation. *J. Atmos. Sci.*, **61**, 296-309,
1229 10.1175/1520-0469(2004)061<0296:SPVHPA>2.0.CO;2.

1230 Lin, J.-L., and Coauthors, 2006: Tropical intraseasonal variability in 14 IPCC AR4
1231 climate models. Part I: Convective signals. *J. Climate*, **19**, 2665-2690,
1232 10.1175/JCLI3735.1.

1233 Lin, X., and R. H. Johnson, 1996: Heating, Moistening, and rainfall over the western
1234 Pacific warm pool during TOGA COARE. *J. Atmos. Sci.*, **53**, 3367-3383,
1235 doi:10.1175/1520-0469(1996)053<3367:HMAROT>2.0.CO;2.

1236 Liu, W. T., K. B. Katsaros, and J. A. Businger, 1979: Bulk parameterization of air-sea
1237 exchanges of heat and water-vapor including the molecular constraints at the
1238 interface. *J. Atmos. Sci.*, **36**, 1722-1735.

1239 Madden, R. A., and P. R. Julian, 1971: Detection of a 40-50 day oscillation in the zonal
1240 wind in the tropical Pacific. *J. Atmos. Sci.*, **28**, 702-708.

1241 Maloney, E. D., and D. L. Hartmann, 1998: Frictional moisture convergence in a
1242 composite life cycle of the Madden–Julian Oscillation. *J. Climate*, **11**, 2387-2403,
1243 10.1175/1520-0442(1998)011<2387:FMCIAC>2.0.CO;2.

1244 Maloney, E. D., and J. T. Kiehl, 2002: MJO-Related SST variations over the tropical
1245 eastern Pacific during Northern Hemisphere summer. *J. Climate*, **15**, 675-689,
1246 doi:10.1175/1520-0442(2002)015<0675:MRSVOT>2.0.CO;2.

1247 Maloney, E. D., 2009: The moist static energy budget of a composite tropical
1248 intraseasonal oscillation in a climate model. *J. Climate*, **22**, 711-729,
1249 10.1175/2008JCLI2542.1.

1250 Majda, A. J., and S. N. Stechmann, 2009: The skeleton of tropical intraseasonal

1251 oscillations. *Proceedings of the National Academy of Sciences*, **106**, 8417-8422,
1252 10.1073/pnas.0903367106.

1253 Mapes, B. E., and R. A. Houze, 1995: Diabatic Divergence profiles in western Pacific
1254 mesoscale convective systems. *J. Atmos. Sci.*, **52**, 1807-1828, 10.1175/1520-
1255 0469(1995)052<1807:ddpiwp>2.0.co;2.

1256 Marion, J. R., 2014: Providing the best turbulent heat flux estimates from eddy
1257 correlation and bulk methods using DYNAMO data, College of Earth, Ocean, and
1258 Atmospheric Sciences, Oregon State University.

1259 Marshall, A. G., O. Alves, and H. H. Hendon, 2008: An enhanced moisture convergence–
1260 evaporation feedback mechanism for MJO air-sea interaction. *J. Atmos. Sci.*, **65**,
1261 970-986, 10.1175/2007JAS2313.1.

1262 Matsuno, T., 1966: Quasi-geostrophic motions in the equatorial area. *J. Meteor. Soc.*
1263 *Japan*, **44**, 25-43.

1264 McPhaden, M. J., and Coauthors, 1992: The response of the western equatorial Pacific
1265 Ocean to westerly wind bursts during November 1989 to January 1990. *Journal of*
1266 *Geophysical Research: Oceans*, **97**, 14289-14303, 10.1029/92JC01197.

1267 Moran, K. P., and Coauthors, 2012: A motion stabilized W-band radar for shipboard
1268 cloud observations and airborne studies of sea spray. *Journal of Boundary Layer*
1269 *Meteorology*, **143**, 3-24, 10.1007/s10546-011-9674-5.

1270 Moum, J. N., and Coauthors, 2014: Air-sea interactions from westerly wind bursts during
1271 the November 2011 MJO in the Indian Ocean. *Bull. Amer. Meteorol. Soc.*,
1272 10.1175/BAMS-D-12-00225.1.

1273 Neelin, J. D., I. M. Held, and K. H. Cook, 1987: Evaporation-wind feedback and low-

1274 frequency variability in the tropical atmosphere. *J. Atmos. Sci.*, **44**, 2341-2348,
1275 doi:10.1175/1520-0469(1987)044<2341:EWFALF>2.0.CO;2.

1276 Neelin, J. D., and N. Zeng, 2000: A quasi-equilibrium tropical circulation model—
1277 formulation. *J. Atmos. Sci.*, **57**, 1741-1766, doi:10.1175/1520-
1278 0469(2000)057<1741:AQETCM>2.0.CO;2.

1279 Negri, A. J., T. L. Bell, and L. Xu, 2002: Sampling of the diurnal cycle of precipitation
1280 using TRMM. *J. Atmos. and Oceanic Tech.*, **19**, 1333-1344, 10.1175/1520-
1281 0426(2002)019<1333:SOTDCO>2.0.CO;2.

1282 North, G. R., T. L. Bell, R. F. Cahalan, and F. J. Moeng, 1982: Sampling errors in the
1283 estimation of empirical orthogonal functions. *Mon. Wea. Rev.*, **110**, 699-706,
1284 10.1175/1520-0493(1982)110<0699:SEITEO>2.0.CO;2.

1285 O'Neill, L. W., S. Wang, and Q. Jiang, 2011: Satellite climatology of cloud liquid water
1286 path over the Southeast Pacific between 2002 and 2009. *Atmospheric Chemistry
1287 and Physics Discussions*, **11**, 31159-31206, 10.5194/acpd-11-31159-2011.

1288 Praveen Kumar, B., J. Vialard, M. Lengaigne, V. S. N. Murty, and M. J. McPhaden,
1289 2012: TropFlux: air-sea fluxes for the global tropical oceans—description and
1290 evaluation. *Climate Dynamics*, **38**, 1521-1543, 10.1007/s00382-011-1115-0.

1291 Price, J. F., R. A. Weller, and R. Pinkel, 1986: Diurnal cycling: Observations and models
1292 of the upper ocean response to diurnal heating, cooling, and wind mixing. *Journal
1293 of Geophysical Research: Oceans*, **91**, 8411-8427, 10.1029/JC091iC07p08411.

1294 Reynolds, R. W., N. A. Rayner, T. M. Smith, D. C. Stokes, and W. Wang, 2002: An
1295 improved in situ and satellite SST analysis for climate. *J. Climate*, **15**, 1609-1625.

1296 Reynolds, R. W., T. M. Smith, C. Liu, D. B. Chelton, K. S. Casey, and M. G. Schlax,

1297 2007: Daily high-resolution-blended analyses for sea surface temperature. *J.*
1298 *Climate*, **20**, 5473-5496, 10.1175/2007JCLI1824.1.

1299 Riehl, H., and J. S. Malkus, 1958: On the heat balance in the equatorial trough zone.
1300 *Geophysica*, **6**, 503-538.

1301 Risien, C. M., and D. B. Chelton, 2008: A global climatology of surface wind and wind
1302 stress fields from eight years of QuikSCAT scatterometer data. *J. Phys.*
1303 *Oceanogr.*, **38**, 2379-2413.

1304 Rui, H., and B. Wang, 1990: Development characteristics and dynamic structure of
1305 tropical intraseasonal convection anomalies. *J. Atmos. Sci.*, **47**, 357-379,
1306 10.1175/1520-0469(1990)047<0357:DCADSO>2.0.CO;2.

1307 Salby, M. L., R. R. Garcia, and H. H. Hendon, 1994: Planetary-scale circulations in the
1308 presence of climatological and wave-induced heating. *J. Atmos. Sci.*, **51**, 2344-
1309 2367, 10.1175/1520-0469(1994)051<2344:PSCITP>2.0.CO;2.

1310 Saunders, P. M., 1967: The temperature at the ocean-air interface. *J. Atmos. Sci.*, **24**, 269-
1311 273, 10.1175/1520-0469(1967)024<0269:TTATOA>2.0.CO;2.

1312 Shinoda, T., H. H. Hendon, and J. Glick, 1998: Intraseasonal variability of surface fluxes
1313 and sea surface temperature in the tropical western Pacific and Indian Oceans. *J.*
1314 *Climate*, **11**, 1685-1702, doi:10.1175/1520-
1315 0442(1998)011<1685:IVOSFA>2.0.CO;2.

1316 Smyth, W. D., D. Hebert, and J. N. Moum, 1996: Local ocean response to a multiphase
1317 westerly wind burst: 2. Thermal and freshwater responses. *Journal of Geophysical*
1318 *Research: Oceans*, **101**, 22513-22533, 10.1029/96jc02006.

1319 Sobel, A. H., and C. S. Bretherton, 2000: Modeling tropical precipitation in a single

1320 column. *J. Climate*, **13**, 4378-4392, 10.1175/1520-
1321 0442(2000)013<4378:MTPIAS>2.0.CO;2.

1322 Sobel, A. H., J. Nilsson, and L. M. Polvani, 2001: The weak temperature gradient
1323 approximation and balanced tropical moisture waves. *J. Atmos. Sci.*, **58**, 3650-
1324 3665, 10.1175/1520-0469(2001)058<3650:twtgaa>2.0.co;2.

1325 Sobel, A. H., E. D. Maloney, G. Bellon, and D. M. Frierson, 2010: Surface fluxes and
1326 tropical intraseasonal variability: a reassessment. *Journal of Advances in*
1327 *Modeling Earth Systems*, **2**, 27, doi:10.3894/JAMES.2010.2.2.

1328 Sobel, A., and E. Maloney, 2012: An idealized semi-empirical framework for modeling
1329 the Madden-Julian Oscillation. *J. Atmos. Sci.*, **69**, 1691-1705, 10.1175/jas-d-11-
1330 0118.1.

1331 Stevens, B., J. Duan, J. C. McWilliams, M. Münnich, and J. D. Neelin, 2002:
1332 Entrainment, Rayleigh friction, and boundary layer winds over the tropical Pacific.
1333 *J. Climate*, **15**, 30-44, 10.1175/1520-0442(2002)015<0030:ERFABL>2.0.CO;2.

1334 Straub, K. H., and G. N. Kiladis, 2003: The observed structure of convectively coupled
1335 kelvin waves: comparison with simple models of coupled wave instability. *J.*
1336 *Atmos. Sci.*, **60**, 1655-1668, 10.1175/1520-
1337 0469(2003)060<1655:TOSOCC>2.0.CO;2.

1338 Sugiyama, M., 2009: The moisture mode in the quasi-equilibrium tropical circulation
1339 model. Part I: Analysis based on the weak temperature gradient approximation. *J.*
1340 *Atmos. Sci.*, **66**, 1507-1523, 10.1175/2008JAS2690.1.

1341 Thompson, E. J., S. A. Rutledge, B. Dolan, and M. Thurai, 2014: Drop size distributions
1342 of convective and stratiform rain over the equatorial Indian and west Pacific

1343 Oceans. *J. Atmos. Sci.*, submitted.

1344 Uppala, S. M., and Coauthors, 2005: The ERA-40 re-analysis. *Quart. J. Roy. Met. Soc.*,

1345 **131**, 2961-3012, 10.1256/qj.04.176.

1346 Waliser, D. E., 2006: Intraseasonal variability. *The Asian Monsoon*, Springer, 203-257.

1347 Wang, B., and H. Rui, 1990: Dynamics of the coupled moist Kelvin–Rossby wave on an

1348 equatorial β -Plane. *J. Atmos. Sci.*, **47**, 397-413, 10.1175/1520-

1349 0469(1990)047<0397:DOTCMK>2.0.CO;2.

1350 Wang, B., and X. Xie, 1998: Coupled modes of the warm pool climate system. Part I:

1351 The role of air-sea interaction in maintaining Madden-Julian oscillation. *J.*

1352 *Climate*, **11**.

1353 Webb, E. K., G. I. Pearman, and R. Leuning, 1980: Correction of flux measurements for

1354 density effects due to heat and water vapour transfer. *Quart. J. Roy. Met. Soc.*,

1355 **106**, 85-100.

1356 Webster, P. J., and R. Lukas, 1992: TOGA COARE: The Coupled Ocean-Atmosphere

1357 Response Experiment. *Bull. Amer. Meteorol. Soc.*, **73**, 1377-1416.

1358 Weller, R. A., and S. P. Anderson, 1996: Surface meteorology and air-sea fluxes in the

1359 western equatorial pacific warm pool during the TOGA Coupled Ocean-

1360 Atmosphere Response Experiment. *J. Climate*, **9**, 1959-1990, doi:10.1175/1520-

1361 0442(1996)009<1959:SMAASF>2.0.CO;2.

1362 Wheeler, M. C., and H. H. Hendon, 2004: An all-season real-time multivariate MJO

1363 index: Development of an index for monitoring and prediction. *Mon. Wea. Rev.*,

1364 **132**, 1917-1932.

1365 Wheeler, M., and G. N. Kiladis, 1999: Convectively coupled equatorial waves: Analysis

1366 of clouds and temperature in the wavenumber-frequency domain. *J. Atmos. Sci.*,
1367 **56**, 374-399.

1368 Woodruff, S., H. Diaz, J. Elms, and S. Worley, 1998: COADS Release 2 data and
1369 metadata enhancements for improvements of marine surface flux fields. *Physics
1370 and Chemistry of the Earth*, **23**, 517-526.

1371 Woolnough, S. J., J. M. Slingo, and B. J. Hoskins, 2000: The relationship between
1372 convection and sea surface temperature on intraseasonal timescales. *J. Climate*,
1373 **13**, 2086-2104, 10.1175/1520-0442(2000)013<2086:trbcas>2.0.co;2.

1374 Woolnough, S. J., F. Vitart, and M. A. Balmaseda, 2007: The role of the ocean in the
1375 Madden–Julian Oscillation: Implications for MJO prediction. *Quart. J. Roy. Met.
1376 Soc.*, **133**, 117-128, 10.1002/qj.4.

1377 Yang, D., and A. P. Ingersoll, 2013: Triggered convection, gravity waves, and the MJO:
1378 A shallow-water model. *J. Atmos. Sci.*, **70**, 2476-2486, 10.1175/JAS-D-12-0255.1.

1379 Yasunaga, K., and B. Mapes, 2012a: Differences between more divergent and more
1380 rotational types of convectively coupled equatorial waves. Part II: Composite
1381 analysis based on space-time filtering. *J. Atmos. Sci.*, **69**, 17-34, 10.1175/JAS-D-
1382 11-034.1.

1383 Yasunaga, K., and B. Mapes, 2012b: Differences between more divergent and more
1384 rotational types of convectively coupled equatorial waves. Part I: Space–time
1385 spectral analyses. *J. Atmos. Sci.*, **69**, 3-16, 10.1175/JAS-D-11-033.1.

1386 Yasunaga, K., and B. Mapes, 2014: Differences between faster versus slower components
1387 of convectively coupled equatorial waves. *J. Atmos. Sci.*, **71**.

1388 Yokoi, S., M. Katsumata, and K. Yoneyama, 2014: Variability in surface meteorology

1389 and air-sea fluxes due to cumulus convective systems observed during
1390 CINDY/DYNAMO. *Journal of Geophysical Research: Atmospheres*, **119**,
1391 2013JD020621, 10.1002/2013JD020621.

1392 Yoneyama, K., C. Zhang, and C. N. Long, 2013: Tracking pulses of the madden–julian
1393 oscillation. *Bull. Amer. Meteorol. Soc.*, **94**, 1871-1891, 10.1175/BAMS-D-12-
1394 00157.1.

1395 Yu, L., and R. A. Weller, 2007: Objectively analyzed air-sea heat fluxes for the global
1396 ice-free oceans (1981-2005).

1397 Zhang, C., and M. J. McPhaden, 2000: Intraseasonal surface cooling in the equatorial
1398 western pacific. *J. Climate*, **13**, 2261-2276, 10.1175/1520-
1399 0442(2000)013<2261:ISCITE>2.0.CO;2.

1400 Zhang, Y. C., W. B. Rossow, A. A. Lacis, V. Oinas, and M. I. Mishchenko, 2004:
1401 Calculation of radiative fluxes from the surface to top of atmosphere based on
1402 ISCCP and other global data sets: Refinements of the radiative transfer model and
1403 the input data. *J. Geophys. Res.*, **109**, D19105.

1404 **Tables**
 1405

1406 **Table 1.** Comparison of OAFlux and TropFlux sensible (SHF) and latent (LHF) heat fluxes
 1407 with *Revelle* surface flux observations.

	mean ($W\ m^{-2}$)		standard deviation		<i>Revelle</i> correlation	
	LHF	SHF	LHF	SHF	LHF	SHF
<i>Revelle</i>	109.0	8.1	32.4	7.0	1	1
OAFlux	106.4	8.3	34.8	5.7	0.87	0.85
TropFlux	111.4	8.8	39.3	8.1	0.84	0.87

1408

1409 **Table 2.** Dates of minimum OLR and SST in intraseasonal events during DYNAMO and
 1410 TOGA COARE.

event	OLR minimum	SST minimum
DYNAMO		
I1	2011 Oct 29	Oct 31
I2	Nov 28	Dec 1
I3	Dec 20	Dec 30
TOGA COARE		
P1	1992 Oct 22, Nov 3 centered Oct 28	Nov 11
P2	1992 Dec 16, 1993 Jan 2 centered Dec 24	Jan 3
P3	Jan 30	Feb 7

1411

1412 **Table 3.** Peak–trough range of daily and intraseasonally filtered OLR and SST in DYNAMO.

1413 Local regression of the first two PCs and RMM indices captures less of the observed daily
 1414 variance. The percentage of the daily OLR peak-to-trough range retained by the filtering and
 1415 regressions on global indices is shown in parentheses.

	Δ OLR	Δ SST
daily	$160\ W\ m^{-2}$	$1.0\ ^\circ C$
15-100 day	110 (68%)	0.9
2 PCs	90 (56%)	0.3
2 RMMs	35 (21%)	0.2

1416 **Table 4.** All-experiment mean (\pm standard errors) of daily heat fluxes and precipitation
 1417 sampled by the IMET buoy data set (Anderson et al. 1996), by the R/V *Moana Wave* in
 1418 TOGA COARE, and by the R/V *Revelle* in DYNAMO. The number of degrees of freedom
 1419 equals the number of days in DYNAMO, but is the number of days divided by 1.5 due to the
 1420 slight autocorrelation of the TOGA COARE daily time series.

1421

DYNAMO vs. TOGA COARE experiment mean surface fluxes (W m^{-2})

	n_{dof}	net	E+H+LW	SW	P
TOGA COARE (1992-1993)					
IMET	88	18 \pm 7	-176 \pm 3	193 \pm 3	324 \pm 46
IMET (<i>MW</i> sampling)	34	23 \pm 12	-171 \pm 6	194 \pm 9	341 \pm 83
<i>Moana Wave</i>	34	29 \pm 13	-168 \pm 6	197 \pm 10	276 \pm 80
DYNAMO (2011-2012)					
<i>Revelle</i>	75	43 \pm 11	-173 \pm 4	216 \pm 9	210 \pm 34

1422

1423 **Table A1.** Summary of primary instrumentation on the *Revelle* in DYNAMO

sensor	variable(s) measured	manufacturer & model	sampling frequency	height
sonic anemometer	3-axis wind components & sonic temperature	Gill R3-100	10 Hz	17.8 m
		Gill R3-50	10 Hz	17.5 m
		Campbell CSAT3	20 Hz	16.9 m
infrared gas analyzer	water vapor	Licor LI-7500	10 Hz	17.2 m
inertial motion unit	linear accelerations and angular rates	Systron Donner MotionPak	10, 20 Hz	17.0 m
		Systron Donner MotionPakII	10 Hz	16.6 m
GPS compass	Heading	Hemisphere Crescent VS100	10 Hz	12.2 m 16.9 m
aspirated RH/T	Air temperature & relative humidity	Vaisala HMT 335	0.1 Hz	15.6 m
		Vaisala PTU 200	1 Hz	16.2 m
barometer	Air pressure	Vaisala PTU 200	1 Hz	8.6 m
pyranometer	Solar (shortwave) radiative flux	Eppley PSP	unknown	20.4 m
		Kipp & Zonen CM21	1 Hz	13 m
pyrgeometer	IR (longwave) radiative flux	Eppley PIR	unknown	20.4 m
		Eppley PIR	0.1 Hz	12.6 m
		Kipp & Zonen CG4	1 Hz	13 m
optical rain gauge	Rainfall rate	STI ORG	0.1 Hz	16.5 m
self-siphoning rain gauge	Rainfall	RM Young 50202	1 Hz	16.5 m
laser altimeter	Wave height	Riegl LD90-3100VHS-FLP	10 Hz	18.5 m
sea-snake thermistor	sea temperature	YSI - 44030	0.1 Hz	-0.1 m
thermosalino-graph	sea temperature and salinity	SeaBird SBE 45 MicroTSG	unknown	-4.9 m
acoustic Doppler current profiler (ADCP)	ocean currents	RDI Narrowband 150 kHz	unknown	-25 m

1424

1425 **Figure Captions**

1426

1427 **Figure 1.** (a) Mean SST for the equatorial Indian and Pacific Oceans (shaded) overlain
1428 by standard deviation of intraseasonal (15-100 day) OLR anomalies (black, contours
1429 above 15 W m^{-2} are shown with an interval of 3 W m^{-2} , yellow contour is 21 W m^{-2}). (b)
1430 Zonal wind stress (shaded) and wind stress vectors from the Scatterometer Climatology
1431 of Ocean Winds (SCOW, Risien and Chelton 2008). The zero zonal wind stress contour
1432 is gray. Contoured standard deviation of intraseasonal zonal wind stress (0.015 N m^{-2} :
1433 dashed, 0.02: light, 0.025: thick). Locations of DYNAMO (80.5°E) and TOGA COARE
1434 (156°E) ship observations used in this paper are marked with yellow stars.

1435

1436 **Figure 2.** TropFlux and OAFlux gridded surface flux products compared with ship
1437 observations (a) from the R/V *Revelle* for DYNAMO in 2011 and (b) from the R/V
1438 *Moana Wave* for TOGA COARE in 1992-1993.

1439

1440 **Figure 3.** The two leading empirical orthogonal functions (EOFs) of OLR averaged from
1441 15°S - 15°N longitude, and the regression of their principal component (PC) time series
1442 onto the latent and sensible heat fluxes from (a,b) OAFlux and (c,d) TropFlux. Latent
1443 heat fluxes follow (are west of) sensible heat flux anomalies. (e-h, shaded) Two-
1444 dimensional spatial pattern regressions on the first two PC time series for TropFlux (e,f)
1445 latent heat flux and (g,h) sensible heat flux. Positive heat flux anomalies indicate upward
1446 heat fluxes out of the ocean. Contours in e-h show the respective EOFs of OLR (interval
1447 2 W m^{-2}).

1448

1449

1450 **Figure 4.** (a,c) OLR and (b,d) SST at the locations of DYNAMO and TOGA COARE
1451 during their respective intensive observation periods. OLR and ERA-I SST anomalies
1452 regressed on the leading two intraseasonal OLR principal components (PC, red dashed)
1453 and the Realtime Multivariate MJO (RMM, orange dot-dashed) indices (Wheeler and
1454 Hendon 2004) underestimate the local daily (thin blue) and intraseasonal (thick blue)
1455 variability observed in TOGA COARE and DYNAMO. Labels I1, I2, I3, P1, P2, and P3
1456 indicate times of low intraseasonally-filtered OLR anomalies. The gray dashed line in
1457 panels a and c corresponds to the right axis and shows the 50-day lowpass filtered
1458 normalized magnitude of the first two principal components of tropical intraseasonal
1459 OLR.

1460

1461 **Figure 5.** Daily average surface heat fluxes incident on the ocean (a, positive warms the
1462 ocean) in DYNAMO, averaged over each local solar day at the equator, 80.5° E. Solar
1463 radiation (blue) is compensated by evaporation (green), longwave radiation (red), and
1464 sensible heat flux (orange), resulting in the net surface heat balance (black). Variations in
1465 cloud fraction (b, clear fraction indicated as blue) and rain from the TOGA precipitation
1466 radar averaged within 20 km of the ship (bars) and ship optical rain gauge (circles). (c)
1467 hourly running mean of 10-minute zonal wind stress. (d) 10-minute 0.1 m depth sea
1468 surface temperature (from the *Revelle* when stationed at 0°N, 80.5°E, orange). Ocean
1469 temperature at 10 m depth from the OSU Ocean Mixing Group Chameleon profiler (dark
1470 red), and the APL buoy (0°N, 79°E) when the ship was off station. Surface air

1471 temperature (blue) measured on the ship in the DYNAMO experiment. Green shading
1472 behind all panels highlights days negative net surface heat flux cooled the ocean.

1473

1474 **Figure 6.** As in Figure 5 but for hourly data from the R/V *Moana Wave* and the IMET
1475 buoy. Wind stress (gray R/V *Moana Wave*, shaded IMET), SST (red line 0.45 m IMET,
1476 dots *Moana Wave*), and air temperature (blue line IMET, dots *Moana Wave*). (IMET data
1477 courtesy S.P. Anderson and R. Weller as in Anderson et al. 1996)

1478

1479 **Figure 7.** Vertical structure of two convectively coupled Kelvin waves that passed over
1480 *Revelle* on November 24-25 and November 27-28. Time increases from right to left to
1481 demonstrate the zonal structure of the anomalies as they propagate from west to east.

1482

1483 **Figure 8.** Evaporation versus daily averaged rain rate averaged over several stations from
1484 TOGA COARE and over the 20 km radius radar disk around the *Revelle* in DYNAMO.

1485

1486 **Figure 9.** (a) Hourly total water path (cm liquid water equivalent, or 10^5 kg m^{-2})
1487 retrieved by microwave radiometer from the *Revelle*. (b) Daily column integrated water
1488 budget: precipitation from radar within 20 km range of the ship, evaporation from bulk
1489 flux algorithm, storage from microwave radiometer, and moisture convergence from the
1490 residual.

1491

1492 **Figure 10.** Longitude-phase plots of (a) OLR, (b) SST, (c) SST tendency and (d-h) heat
1493 flux anomalies for 103 strongly eastward-propagating convective events composited by

1494 intraseasonal phase before and after their OLR is minimum at 80°E. Positive fluxes warm
1495 the ocean. The black contours in each panel show the low-OLR anomaly of the
1496 convective phase of the MJO constructed from the first two leading EOFs. White
1497 hatching covers SST and component flux anomalies that are not statistically significant at
1498 95% confidence (except SST tendency is significant only at its peaks, and net surface
1499 heat flux is significant almost everywhere). Like Figures 5 and 6, negative surface heat
1500 fluxes in cool the ocean.

1501

1502 **Figure 11.** MJO composite zonal surface wind stress, turbulence specific humidity scale
1503 q^* , and turbulence temperature scale T^* over the Indian and Pacific Oceans, as in Figure
1504 10.

1505

1506 **Figure 12.** Accumulated precipitation (from in situ ship, IMET, and TAO/RAMA buoys)
1507 and evaporation from the (a) DYNAMO and (b) TOGA COARE experiments.

1508

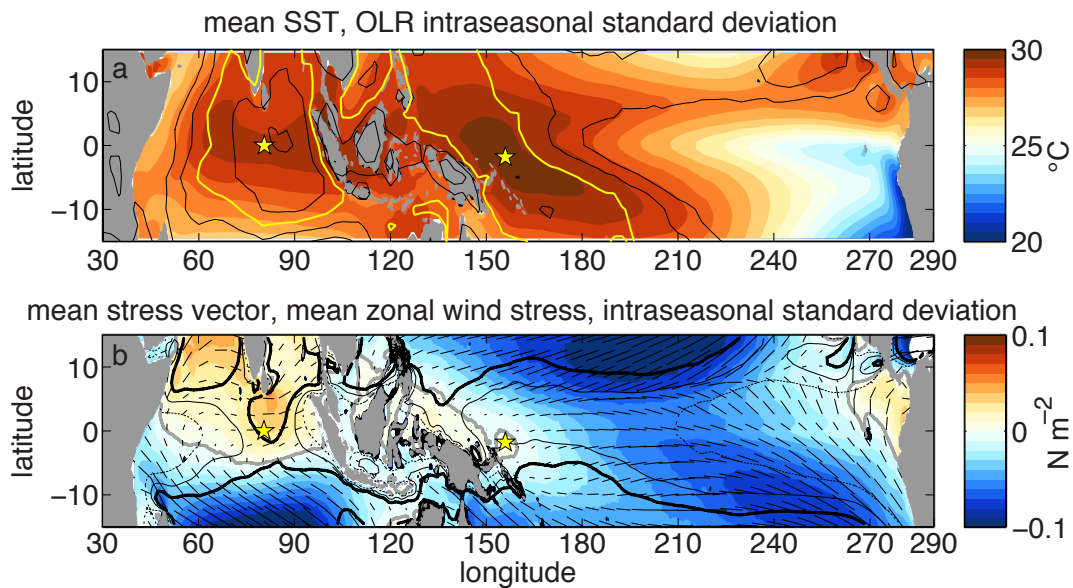


Figure 1. (a) Mean SST for the equatorial Indian and Pacific Oceans (shaded) overlain by standard deviation of intraseasonal (15-100 day) OLR anomalies (black, contours above 15 W m^{-2} are shown with an interval of 3 W m^{-2} , yellow contour is 21 W m^{-2}). (b) Zonal wind stress (shaded) and wind stress vectors from the Scatterometer Climatology of Ocean Winds (SCOW, Risien and Chelton 2008). The zero zonal wind stress contour is gray. Contoured standard deviation of intraseasonal zonal wind stress (0.015 N m^{-2} : dashed, 0.02 : light, 0.025 : thick). Locations of DYNAMO (80.5°E) and TOGA COARE (156°E) ship observations used in this paper are marked with yellow stars.

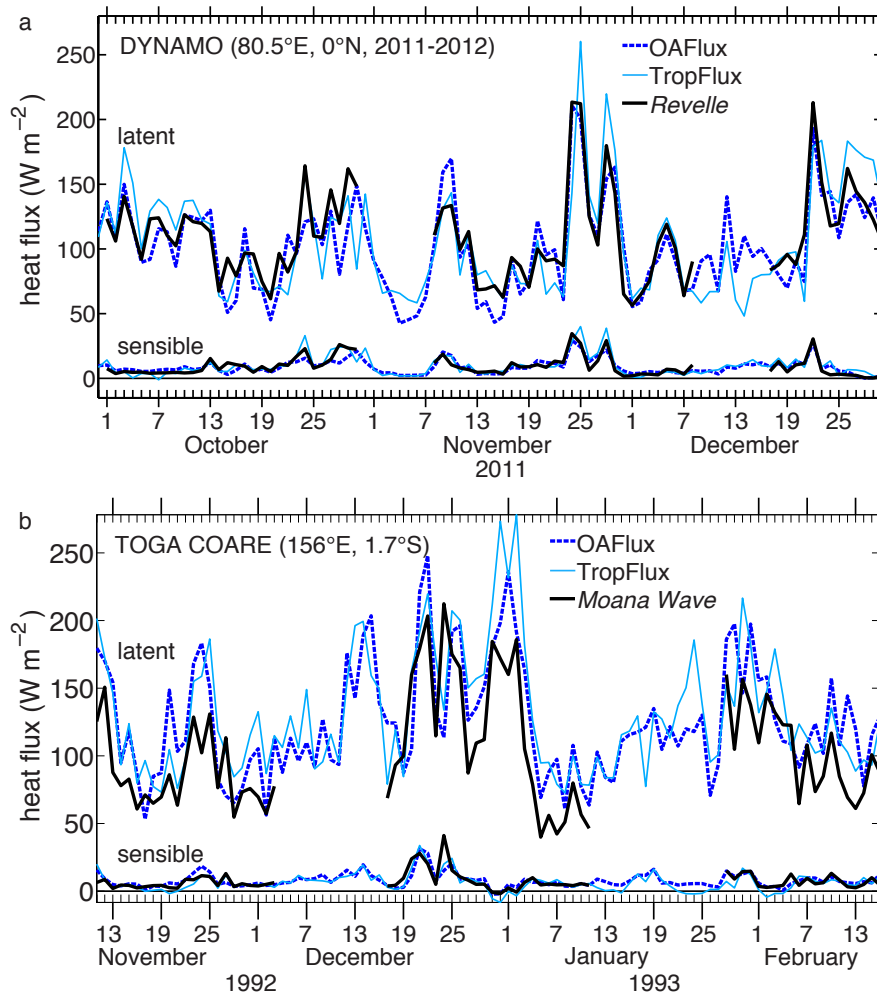


Figure 2. TropFlux and OAFlux gridded surface flux products compared with ship observations (a) from the R/V *Revelle* for DYNAMO in 2011 and (b) from the R/V *Moana Wave* for TOGA COARE in 1992-1993.

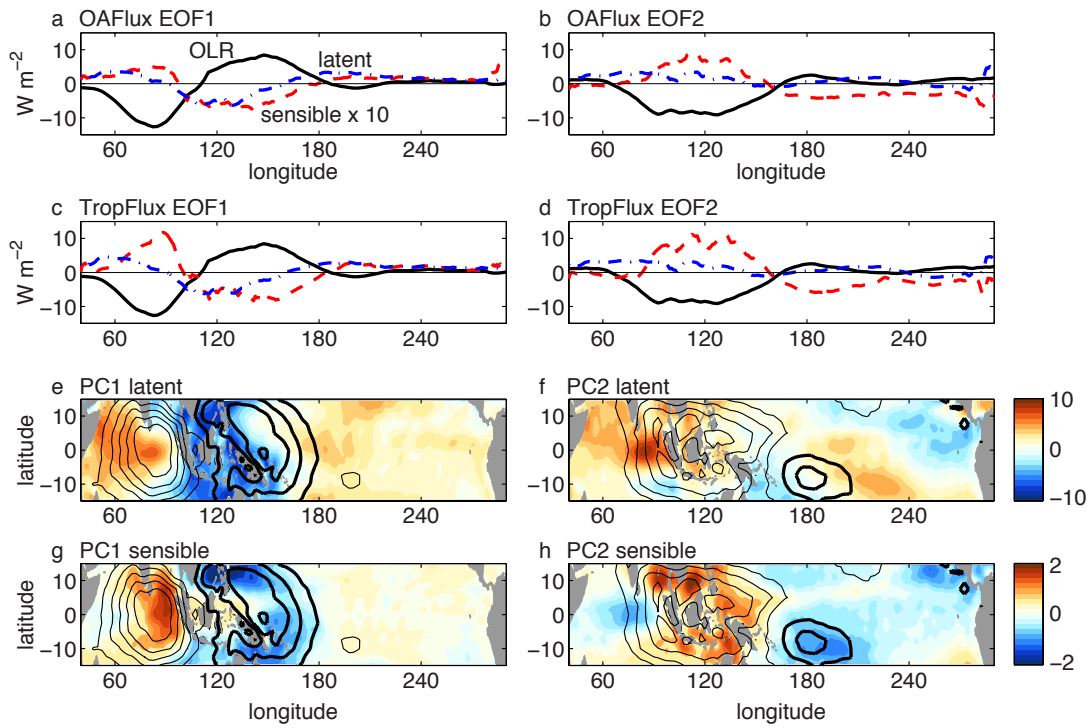


Figure 3. The two leading empirical orthogonal functions (EOFs) of OLR averaged from 15°S - 15°N longitude, and the regression of their principal component (PC) time series onto the latent and sensible heat fluxes from (a,b) OAF flux and (c,d) TropFlux. Latent heat fluxes follow (are west of) sensible heat flux anomalies. (e-h, shaded) Two-dimensional spatial pattern regressions on the first two PC time series for TropFlux (e,f) latent heat flux and (g,h) sensible heat flux. Positive heat flux anomalies indicate upward heat fluxes out of the ocean. Contours in e-h show the respective EOFs of OLR (interval 2 W m^{-2}).

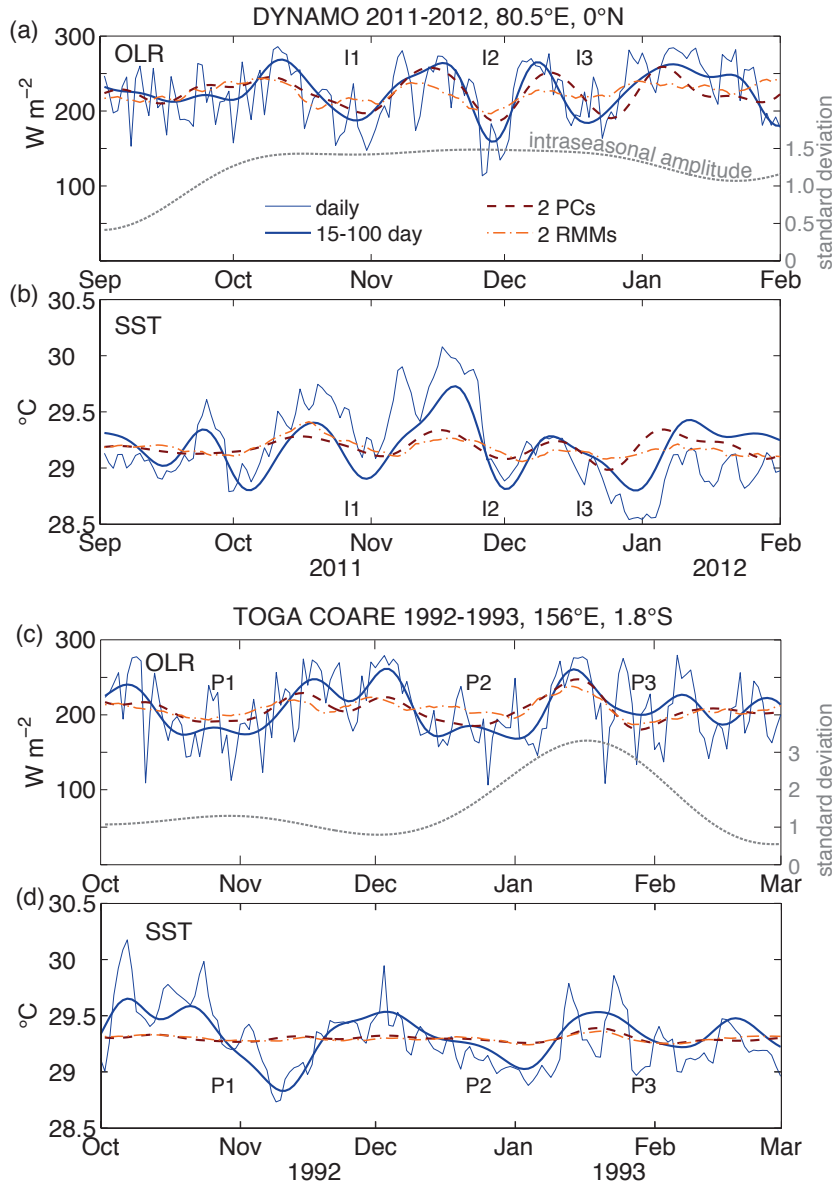


Figure 4. (a,c) OLR and (b,d) SST at the locations of DYNAMO and TOGA COARE during their respective intensive observation periods. OLR and ERA-I SST anomalies regressed on the leading two intraseasonal OLR principal components (PC, red dashed) and the Realtime Multivariate MJO (RMM, orange dot-dashed) indices (Wheeler and Hendon 2004) underestimate the local daily (thin blue) and intraseasonal (thick blue) variability observed in TOGA COARE and DYNAMO. Labels I1, I2, I3, P1, P2, and P3 indicate times of low intraseasonally-filtered OLR anomalies. The gray dashed line in panels a and c corresponds to the right axis and shows the 50-day lowpass filtered normalized magnitude of the first two principal components of tropical intraseasonal OLR.

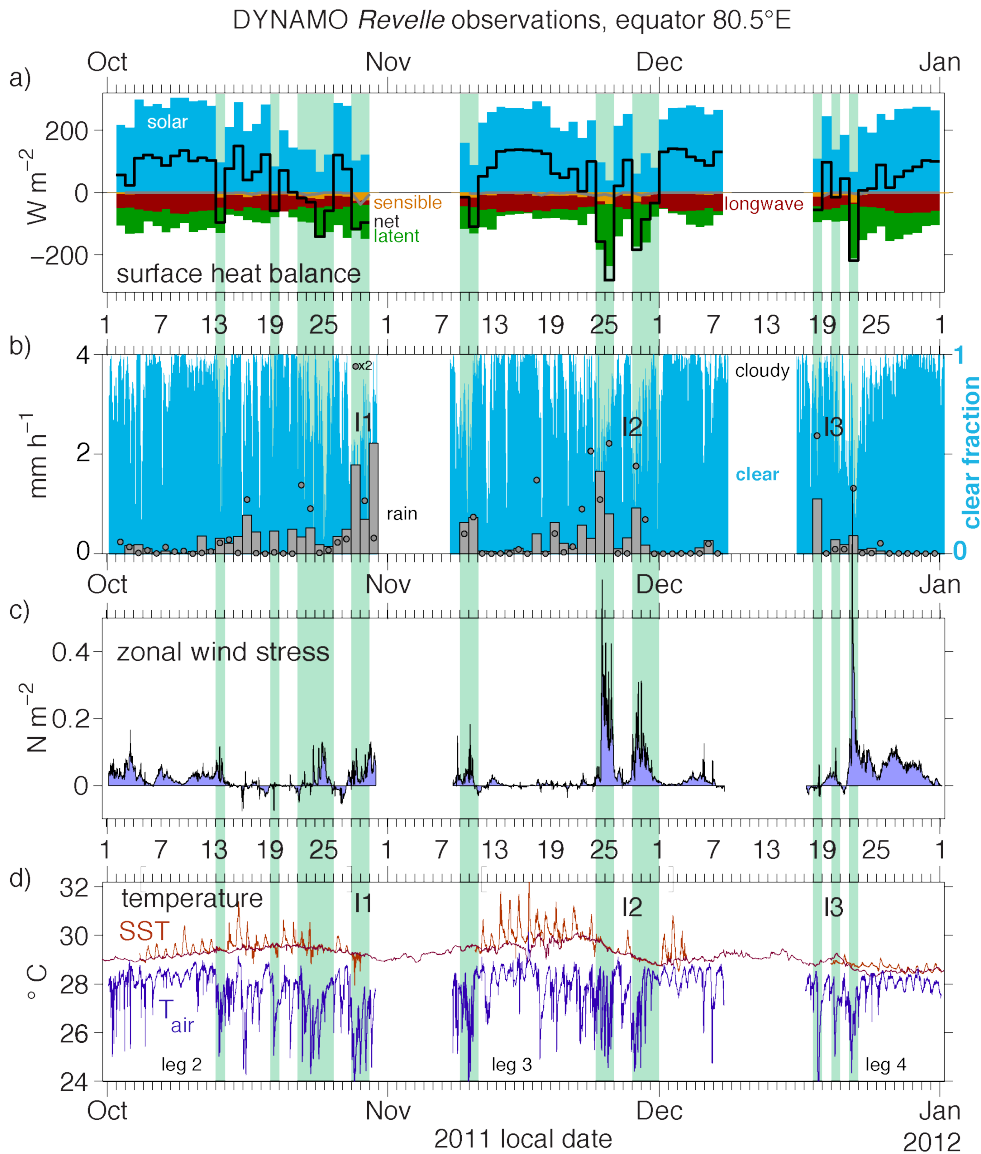


Figure 5. Daily average surface heat fluxes incident on the ocean (a, positive warms the ocean) in DYNAMO, averaged over each local solar day at the equator, 80.5° E. Solar radiation (blue) is compensated by evaporation (green), longwave radiation (red), and sensible heat flux (orange), resulting in the net surface heat balance (black). Variations in cloud fraction (b, clear fraction indicated as blue) and rain from the TOGA precipitation radar averaged within 20 km of the ship (bars) and ship optical rain gauge (circles). (c) hourly running mean of 10-minute zonal wind stress. (d) 10-minute 0.05 m depth sea surface temperature (from the *Revelle* when stationed at 0°N, 80.5°E, orange). Ocean temperature at 10 m depth from the OSU Ocean Mixing Group Chameleon profiler (dark red), and the APL buoy (0°N, 79°E) when the ship was off station. Surface air temperature (blue) measured on the ship in the DYNAMO experiment. Green shading behind all panels highlights days negative net surface heat flux cooled the ocean.

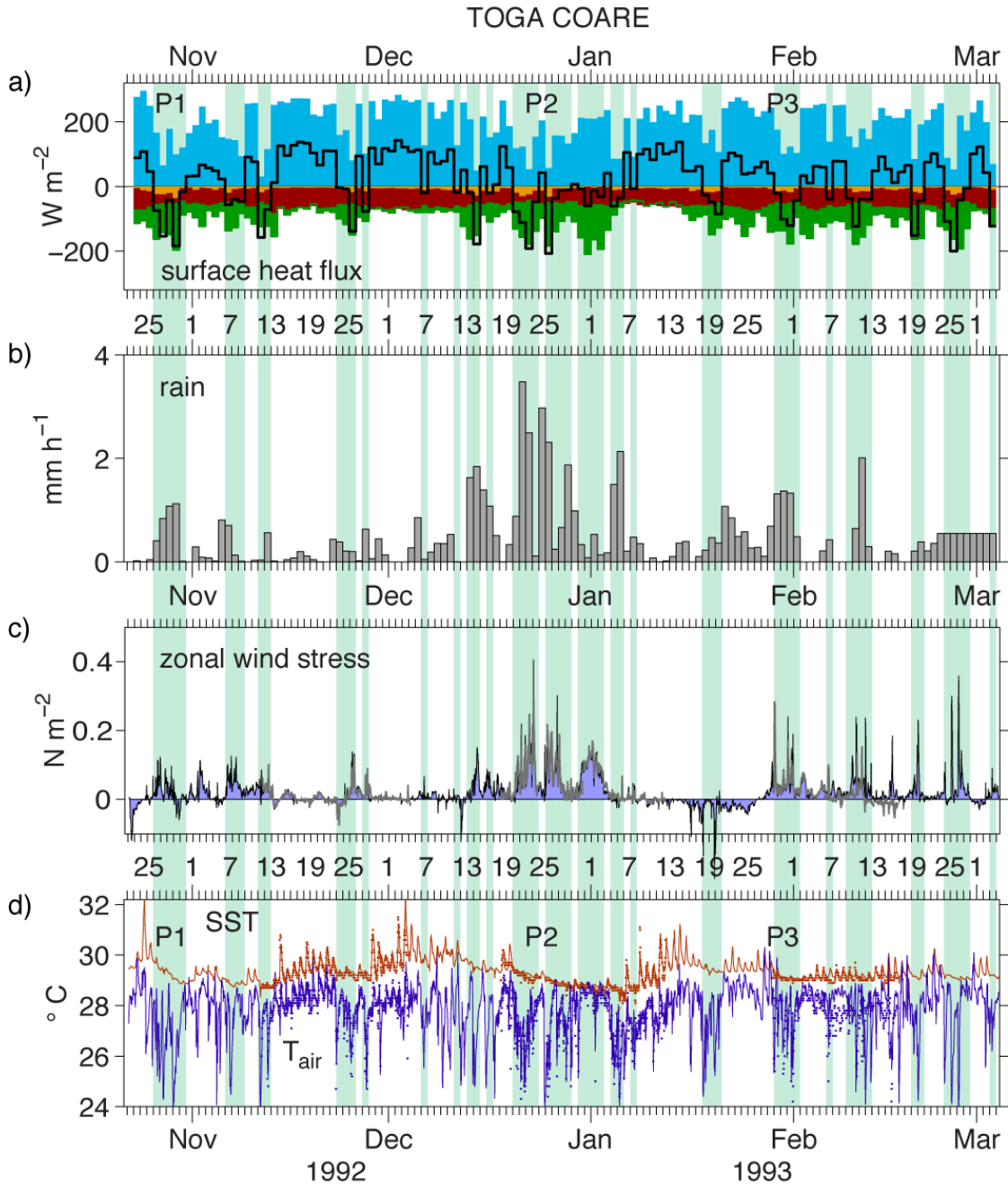


Figure 6. As in Figure 5 but for hourly data from the R/V *Moana Wave* and the IMET buoy. Wind stress (gray R/V *Moana Wave*, shaded IMET), SST (red line 0.45 m IMET, dots *Moana Wave*), and air temperature (blue line IMET, dots *Moana Wave*). (IMET data courtesy S.P. Anderson and R. Weller as in Anderson et al. 1996)

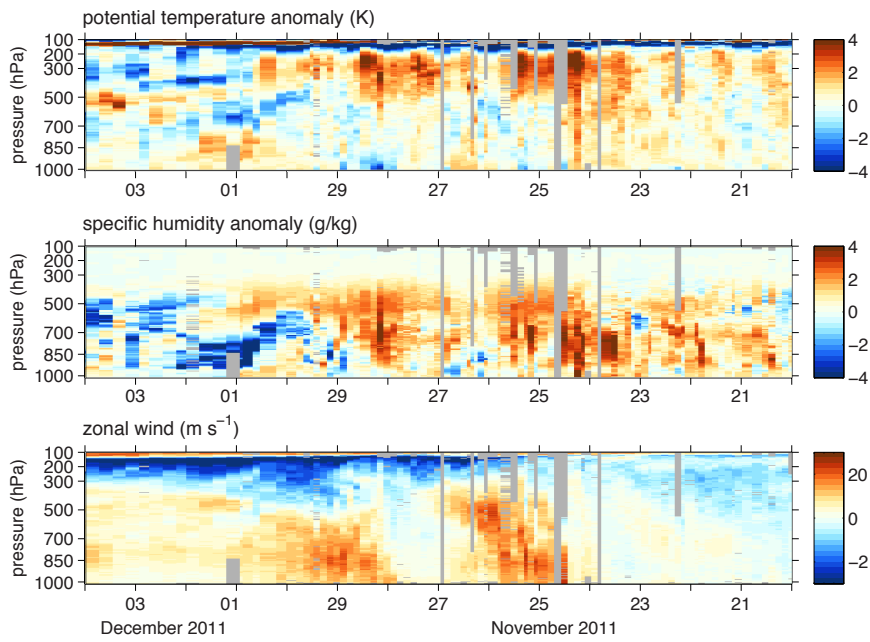


Figure 7. Vertical structure of two convectively coupled Kelvin waves that passed over *Revelle* on November 24-25 and November 27-28. Time increases from right to left to demonstrate the zonal structure of the anomalies as they propagate from west to east.

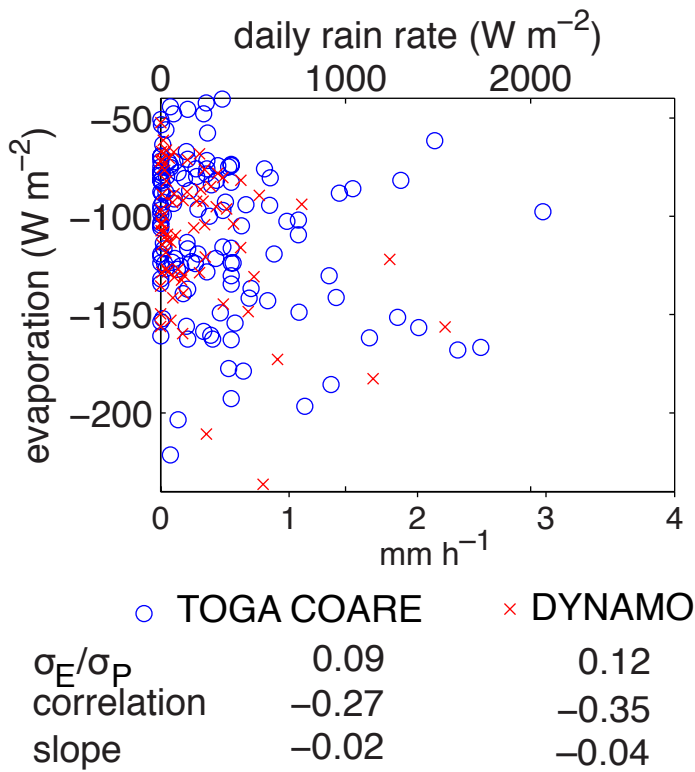


Figure 8. Evaporation versus daily averaged rain rate averaged over several stations from TOGA COARE and over the 20 km radius radar disk around the *Revelle* in DYNAMO.

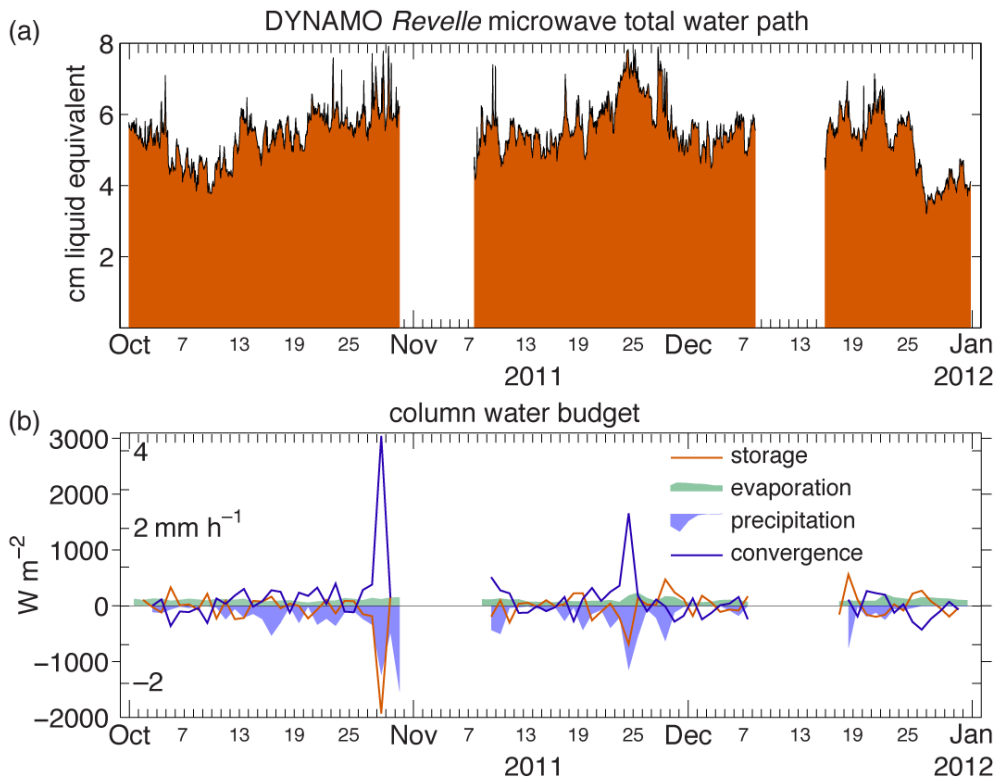


Figure 9. (a) Hourly total water path (cm liquid water equivalent, or 10^5 kg m^{-2}) retrieved by microwave radiometer from the *Revelle*. (b) Daily column integrated water budget: precipitation from radar within 20 km range of the ship, evaporation from bulk flux algorithm, storage from microwave radiometer, and moisture convergence from the residual.

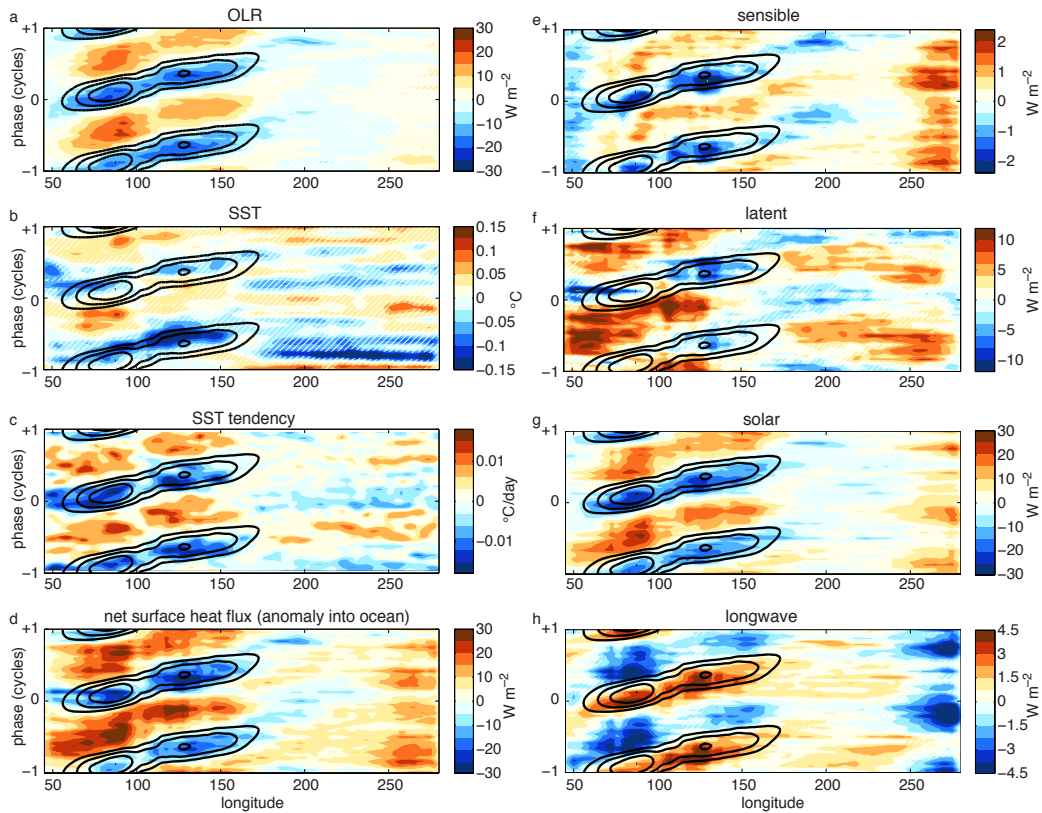


Figure 10. Longitude-phase plots of (a) OLR, (b) SST, (c) SST tendency and (d-h) heat flux anomalies for 103 strongly eastward-propagating convective events composited by intraseasonal phase before and after their OLR is minimum at 80°E . Positive fluxes warm the ocean. The black contours in each panel show the low-OLR anomaly of the convective phase of the MJO constructed from the first two leading EOFs. White hatching covers SST and component flux anomalies that are not statistically significant at 95% confidence (except SST tendency is significant only at its peaks, and net surface heat flux is significant almost everywhere). Like Figures 5 and 6, negative surface heat fluxes in cool the ocean.

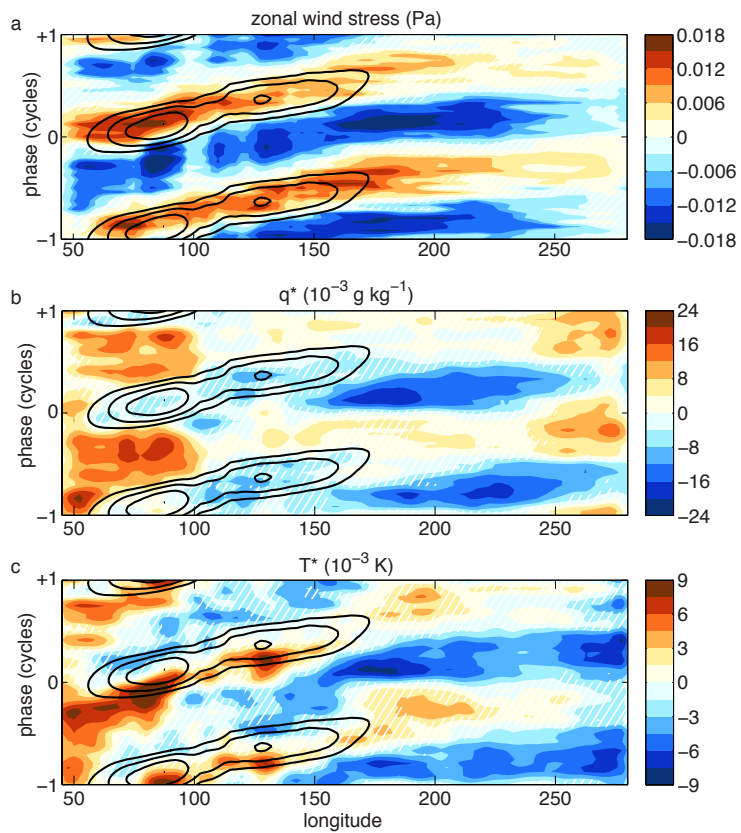


Figure 11. MJO composite zonal surface wind stress, turbulence specific humidity scale q^* , and turbulence temperature scale T^* over the Indian and Pacific Oceans, as in Figure 10.

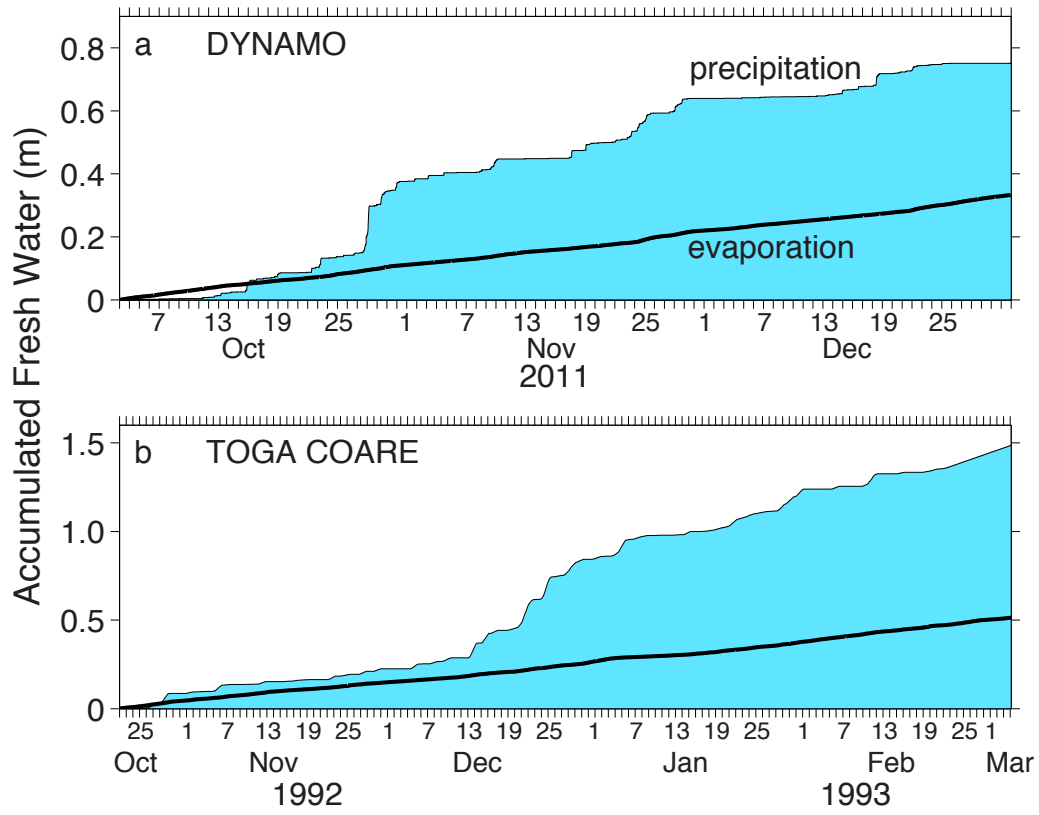


Figure 12. Accumulated precipitation (from in situ ship, IMET, and TAO/RAMA buoys) and evaporation from the (a) DYNAMO and (b) TOGA COARE experiments.